THESIS

SINGLE-NANOFLAKE PHOTOELECTROCHEMISTRY OF $MoSe_2$ THIN FILMS

Submitted by

Allan Edward Isenberg

Department of Chemistry

In partial fulfillment of the requirements

For the Degree of Master of Science

Colorado State University

Fort Collins, Colorado

Spring 2018

Master's Committee:

Advisor: Justin Sambur

James Neilson
Jose de la Venta

ABSTRACT

SINGLE-NANOFLAKE PHOTOELECTROCHEMISTRY OF $MoSe_2$ THIN FILMS

Transition metal dichalcogenide (TMD) thin films represent promising materials for large-area, low-cost, and high-efficiency photoelectrochemical solar energy conversion applications. The outstanding efficiency of bulk TMD crystals has been well documented, which has driven interest in large-area exfoliated TMD thin film devices in recent years. Unfortunately, the solar energy conversion efficiency of nanoflake-coated electrodes is typically much worse than bulk crystal electrodes. It is currently unclear how the high degree of variability among nanoflakes (e.g. area, thickness, types structural features, etc.) contribute to the efficiency gap between nanoflake and bulk electrodes. It is also unclear if exfoliated nanoflakes can achieve the solar conversion efficiencies demonstrated by bulk crystals.

The semiconductor-electrolyte dynamics of TMD/iodide photoelectrochemical cells has also been characterized in bulk systems. Bulk TMD electrodes in an iodide electrolyte will form adsorbed oxidation products at the TMD surface, which can cause sharp drops in efficiency in these systems. A clear understanding of how this phenomenon affects the local photoelectrochemical response has not been established. Additionally, it is not clear how the surface reaction kinetics of iodide oxidation products are affected by surface structural features (e.g. basal planes, perimeter-edges, and interior step edges) on TMD nanoflakes.

Here, a single-nanoflake photoelectrochemical approach is used to establish the existence of highly active champion and inactive spectator nanoflakes in mechanically exfoliated $MoSe_2$ thin films. In the samples studied, 7% of nanoflakes are highly active champions, whose solar conversion efficiencies exceed that of the bulk crystal. Though, 68% of the deposited nanoflakes are inactive spectators, and contribute substantially to the lower photocurrent efficiencies of nanoflake-coated electrodes compared to bulk electrodes. Structural features are also shown to have a significant effect on photocurrent collection efficiencies. Photocurrent collection response is shown to increase with nanoflake area and is more negatively affected by perimeter edges than interior step edges. Moreover, local photoelectrochemical spot measurements show that while adsorbed iodide oxidation products can form at any type of surface structure, these films preferentially form at the most catalytically active and thermodynamically favorable sites for iodide oxidation. These observations reveal previously hidden performance issues associated with exfoliated TMD thin films and highlights performance aspects that can be improved upon.

ACKNOWLEDGEMENTS

I'd first like to acknowledge Justin, who has been the best advisor I could have gotten and has pushed me to be the best that I can be. To all the members of the Sambur Lab, especially the grad students: It has been a pleasure working with and becoming friends with you all. Thank you for making this experience so fun. Finally, I'd like to acknowledge Mary for her unwavering support in my ambitions. I would not have been able to do this without you. Now it's your turn!

DEDICATION

This work is dedicated to Mom and Dad.

Thank you for everything you've done.

TABLE OF CONTENTS

ABSTRACT ii

ACKNOWLEDGEMENTS iv

DEDICATION v

1. Introduction 8

2. Single-Nanoflake Photoelectrochemistry Reveals “Champion” and “Spectator” Exfoliated $MoSe_2$ Nanoflake Thin Films 13

2.1. Synopsis 13

2.2. Introduction 14

2.3. Experimental Methods 15

2.3.1. Bulk Electrode Preparation and Characterization 15

2.3.2. Nanoflake Electrode Preparation 16

2.3.3. Photocurrent Mapping and Raman Micro-spectroscopy 17

2.3.4. Scanning Kelvin Probe Microscopy and Auger Micro-spectroscopy of Exfoliated Nanoflakes 18

2.4. Results and Discussion 19

2.5. Conclusions 38

3. Single-Nanoflake Investigation of Iodine Film Formation on Mechanically Exfoliated $MoSe_2$ Nanoflakes 39

3.1. Synopsis 39

3.2. Introduction 39

3.3. Results and Discussion 41

3.4. Conclusion 49

4. Outlook 50

5. References 52

1. Introduction

1.1. The Chemical, Electronic, and Structural Properties of Transition Metal Dichalcogenides

Transition metal dichalcogenides (TMDs) are a class of compounds with the formula MX_2 where M is a transition metal and X is a chalcogen. Bulk TMDs are composed of three-atom thick X-M-X layers that are held together by Van der Waals forces, with interlayer distances ranging from 0.62-0.75 nm depending on the identities of M and X.[1] TMDs exist in several different crystal structures, but the most common are the so-called 1T, 2H, and 3R phases. The number denotes the number of stacked layers in the unit cell, and T (tetragonal), H (hexagonal), and R (rhombohedral) represent the crystal symmetry around the transition metal atom. Figure 1.1 shows the layered structure of 2H $MoSe_2$. The different crystal phases result in unique chemical and electronic properties between TMDs. For example, the 2H phase of WS_2 is semiconducting, with a thickness dependent band gap ranging from 1.35 to 1.89 eV.[2, 3] However, the 1T phase is metallic.[4] In this way, the crystal structure significantly affects the properties of TMDs, and thus dictates their function.

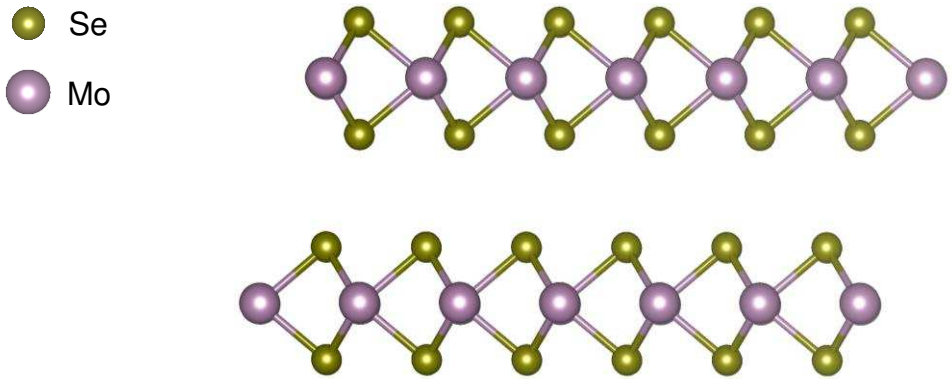

Figure 1.1. TMD crystal structure. The layered structure of 2H $MoSe_2$ looking parallel to the Se-Mo-Se layers. In the 2H phase, consecutive layers are slightly offset from each other, resulting in a unit cell composed of two layers.

1.2. The Photoelectrochemical Properties of TMDs

The optoelectronic properties of TMDs were studied in semiconductor-liquid junction photoelectrochemical cells because a pristine crystal surface could be easily exposed by mechanical exfoliation of the outermost layers, leaving behind clean surfaces. Figure 1.2. shows an energy diagram of a typical photoelectrochemical cell composed of an n-type semiconductor. In a photoelectrochemical cell, a semiconductor is put in direct contact with an electrolyte. Before contact, the electrochemical potentials of the semiconductor (i.e., the Fermi level, or E_F) is more negative than the electrochemical potential of the redox couple in the electrolyte, E^0. When the semiconductor-electrolyte junction is formed, these chemical potentials reach equilibrium. This is achieved by mobile charges migrating from inside the semiconductor to the electrolyte. In this case, E_F of the semiconductor is at a higher energy than the E^0 of the electrolyte, so electrons

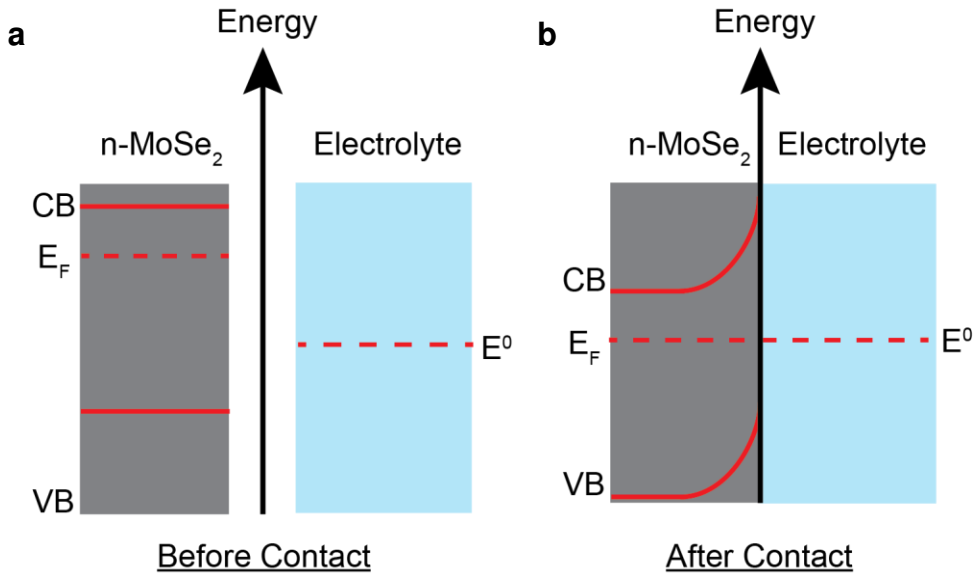

Figure 1.2. A band energy diagram for a photoelectrochemical cell with $MoSe_2$ before semiconductor-electrolyte contact (a) and after contact (b). After contact, the E_F and E^0 of the semiconductor and electrolyte, respectively, equilibrate via the movement of charge carriers. This creates stationary charges inside the semiconductor and an oppositely charged Helmholtz layer of ions at the junction. This creates an electric field that lowers the energy of the valence band (VB) and conduction band (CB) in the semiconductor, thus inducing band bending.

are transferred to the electrolyte. This lowers E_F, bringing the two to equilibrium. This movement of charges leaves behind a space charge region containing stationary charges. The charge imbalance generates a potential drop and an electric field inside the semiconductor that causes spatial variation of the energy of the valence and conduction bands. This phenomenon is called band bending. The dynamics at a semiconductor-electrolyte junction are similar to those of semiconductor-metal junction, also known as a Schottky-Junction, and can be treated the same. In this case, the redox potential of the electrolyte is analogous to the Fermi level of the metal. In a Schottky-Junction, charge carriers are exchanged between the semiconductor and the metal to equilibrate the E_F on both sides of the interface. This creates the potential drop that induces band bending in the semiconductor.

Similarly, the build-up of charges inside the semiconductor attracts ions of opposite charge in the electrolyte, creating a charged Helmholtz layer. This layer also creates a small potential drop, and so affects the band bending in the semiconductor. The band bending in the semiconductor allows for photogenerated charge carriers to be separated. In the case of n-type $MoSe_2$ in an I^-/ I_3^- redox couple, holes are extracted to the $MoSe_2$-electrolyte junction to oxidize I^- to I_3^-, while electrons are extracted in to the circuit. Figure 1.3 shows a $MoSe_2$ | I^-/ I_3^- | Pt regenerative photoelectrochemical cell. In this type of photoelectrochemical cell, the electrons ultimately reduce I_3^- to I^- at the Pt counter, thus keeping the electrolyte composition constant. One of the benefits of the liquid junction photovoltaic is that the semiconductor-electrolyte junction can be directly illuminated. This is beneficial because many charge carriers will be generated in or near the space charge region, which allows for very efficient charge carrier separation and

collection. The result is a device that can achieve high efficiency relatively easily. For example, in 1985, Tenne and co-workers achieved 14.3% efficiency by photoetching the surface of n-WSe_2.[5] Additionally, Prasad and co-workers achieved 17.1% efficiency using a similar surface etching technique three years later.[6] These early observations demonstrate the potential of TMD based photoelectrochemical cells to be highly efficient, low-cost photovoltaics.

1.3. Nanometer Thick TMDs: an Emerging Class of Materials for Solar Energy Conversion

Interest in TMDs stagnated for several years, but excitement in the compounds was reignited after the discovery of monolayer graphene, which also has a layered structure. Considering the high efficiency achieved by bulk crystals when used in photovoltaics, ultra-thin TMDs have great potential to be fabricated in to high-efficiency, large-area, low-cost solar energy conversion devices that could help with the growing need for renewable energy technologies. Using the same exfoliation method used to

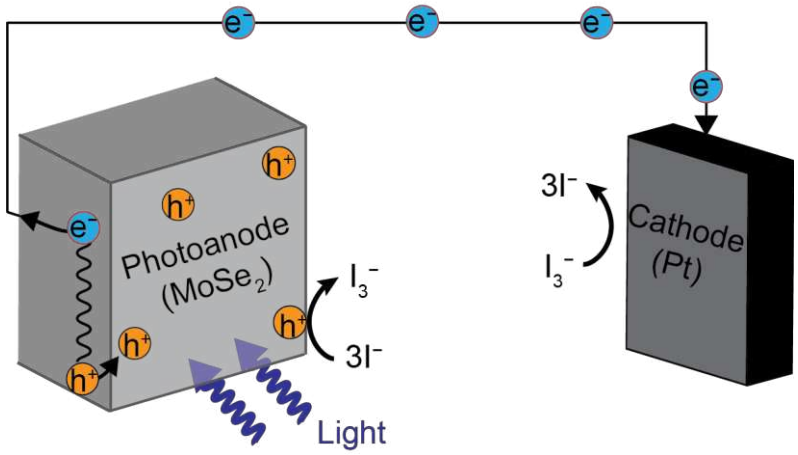

Figure 1.3. An example of a regenerative $MoSe_2$ | I^-/ I_3^- | Pt photoelectrochemical cell. Incident light is absorbed at the semiconducting photoanode (n-$MoSe_2$). Electron-hole pairs are separated by electric fields in the semiconductor. Photogenerated holes are swept to the semiconductor-electrolyte junction where they oxidize I^- to I_3^-. Electrons are extracted in to the circuit, and ultimately reduce I_3^- to I^- at the Pt counter electrode, regenerating the electrolyte.

generate monolayer graphene, groups were able to fabricate nanoflakes of TMDs.[7, 8] New top-down exfoliation techniques were also developed, including solvent assisted exfoliation, which could easily generate large quantities of ultra-thin TMD samples.[9-11] However, exfoliation comes with unique challenges for preparation of samples appropriate for the intended application. Mechanical exfoliation can produce high quality nanoflakes, with monolayer nanosheets possible. However, this a low throughput technique with little to no control over nanoflake dimensions. This makes large-area thin films impossible. Liquid exfoliation techniques using surfactants can produce large amounts of few-layer nanosheets, but reproducibility is low due to the large number of parameters that need to be closely monitored (temperature, sonication time, sonication intensity, surfactant medium, etc.).[12] Additionally, liquid phase exfoliation by intercalation of tert-butyl lithium, or other similar small molecules, often leads to a phase change from semiconducting 2H to metallic 1T in TMDs.[13, 14] This makes photovoltaic devices, which rely on the semiconducting phase to function, made from this exfoliation technique impractical since the nanosheets would need to be converted back to the semiconducting phase.

2. Single-Nanoflake Photoelectrochemistry Reveals “Champion” and “Spectator” Exfoliated $MoSe_2$ Nanoflake Thin Films[i]

2.1. Synopsis

Semiconducting transition metal dichalcogenide (TMD) nanoflake thin films are promising large-area electrodes for photoelectrochemical solar energy conversion applications. However, their energy conversion efficiencies are typically much lower than those of bulk electrodes. It is unclear to what extent this efficiency gap stems from the intrinsic differences among nanoflakes (e.g., area, thickness, and surface structural features). It is also unclear whether individual exfoliated nanoflakes can achieve similar energy conversion efficiencies to those of bulk crystals. Here, we use a single-nanoflake photoelectrochemical approach to demonstrate that there are both highly active and completely inactive nanoflakes within a mechanically exfoliated thin film. For the mechanically exfoliated $MoSe_2$ samples studied herein, 7% of nanoflakes are highly active ”champions”, whose photocurrent efficiencies exceed that of the bulk crystal. However, ~68% of nanoflakes are inactive ”spectators”, which are mostly responsible for the lower average photocurrent efficiency compared to the bulk crystal. Additionally, it was observed that the photocurrent collection efficiency increases with nanoflake area and decreases more at perimeter edges than at interior step edges. These observations, which are hidden in ensemble-level measurements, reveal underlying performance issues of exfoliated TMD electrodes used for photoelectrochemical solar energy conversion applications.

[i] This chapter was prepared as the manuscript Todt, M. A.; Isenberg, A. E.; Nanayakkara, S. U.; Miller, E. M.; Sambur, J. B. *J. Phys. Chem. C.* **2018** *accepted*

2.2. Introduction

Transition metal dichalcogenides (TMDs) such as MoX_2 and WX_2 (where X=S, or Se) are highly efficient and stable electrode materials for photoelectrochemical solar energy conversion to electricity[15-18] and chemical fuels.[19-23] Seminal work in the 1980s demonstrated >10% solar-to-electrical energy conversion efficiency using bulk n-WSe_2 | I^-/I_3^- | Pt solar cells.[5, 6, 24] However, these cells employed small <1.0 cm^2 single crystal electrodes. Thus, there is a strong interest in developing large-area TMD electrodes for large scale energy conversion applications.[25, 26]

One approach to make large-area TMD electrodes is to exfoliate high quality bulk crystals into nanoflakes and deposit them onto conducting substrates.[26, 27] This strategy potential allows for the nanoflakes to retain the excellent energy conversion properties of the parent bulk crystal. Towards this goal, Sivula and co-workers developed a liquid exfoliation method to deposit WSe_2 nanoflake films onto $Sn:In_2O_3$ (ITO) substrates.[10] Their work represents a significant step forward towards large-area TMD electrodes, but the nanoflake film electrode showed lower photocurrent density for hydrogen evolution than bulk WSe_2. Recent simulations show that charge carrier recombination at nanoflake edges likely limits the photocurrent density.[28] However, the origin of the efficiency gap and the extent the poor performance stems from efficiency variations among nanoflakes are not well known. A major unanswered question is whether exfoliated nanoflakes can achieve the energy conversion efficiencies of bulk crystals.

The first step towards understanding how variations among nanoflake impact the overall electrode performance is to measure their photoelectrochemical properties at the single-nanoflake level. Dryfe and co-workers recently reported thickness dependent

electron transfer kinetics for single MoS_2 nanoflakes.[7] The authors made electrical contacts to individual nanoflakes and then placed ~25 μm diameter electrolyte droplets onto their surfaces for single-nanoflake photoelectrochemical measurements. The photocurrent response in this geometry stems from photogenerated carriers that react at surface sites within the microdroplet rather than at all possible surface sites. Since the electrolyte droplet only contacted basal planes, it is unclear how surface motifs affected the photocurrent response. It is critical to study the role of perimeter edge sites because they have been shown to either increase[29, 30] or decrease the performance of TMD electrodes.[18, 28, 31-33]

Here, we demonstrate a single-nanoflake scanning photocurrent microscopy approach to map the external quantum efficiency (EQE) of 59 nanoflakes with 1 μm^2 spatial resolution in n-$MoSe_2$ | I^-/I_3^- | Pt cells. The general operating principles of these photoelectrochemical solar cells are as follows: photogenerated holes within the semiconductor are transported to the interface and oxidize I^-, while electrons are extracted from the semiconductor interior and eventually reduce I_3^- at the Pt cathode. The oxidation reaction is the reverse of the of the reduction reaction at the cathode and there is no net change in the electrolyte composition. Our study focuses on understanding how variations among exfoliated nanoflakes contribute to the overall photocurrent response from the thin film electrode.

2.3. Experimental Methods

2.3.1. Bulk Electrode Preparation and Characterization

Bulk $MoSe_2$ crystals were generously provided by Dr. Bruce Parkinson. The crystals were grown via chemical vapor transport methods described by Kline *et al.*[10] Bulk

crystals were contacted with In/Ga eutectic, mounted onto ITO electrodes, sealed with Loctite Epoxy, and immersed into a single compartment cell containing 1M NaI, 1mM I_2 electrolyte. Electrochemical measurements were performed with an Ivium Compactstat Potentiostat in a 3-electrode configuration (Pt wire counter electrode and Ag/AgI reference electrode). Mott-Schottky analysis showed that the crystals exhibited n-type conductivity with a carrier concentration of 8×10^{16} cm^{-3} and a flatband potential of +0.29 V versus a Ag/AgI reference electrode (Figure 2.1).

2.3.2. Nanoflake Electrode Preparation

Nanoflake $MoSe_2$ samples were exfoliated from bulk crystal samples with cellophane tape and transferred onto 3" × 1" ITO coated glass slides (4-10 Ω, Delta Technologies), similar to methods described by Huang *et al.*[34] A 3-electrode electrochemical flow cell was constructed according to the scheme in Figure 2.2. An approximately 80 μm thick channel was formed by placing a glass cover slip on two pieces of double-sided tape. The edges were sealed using Loctite epoxy. Pre-drilled holes in the ITO slide provide inlet and outlet ports for electrolyte solution to flow through the

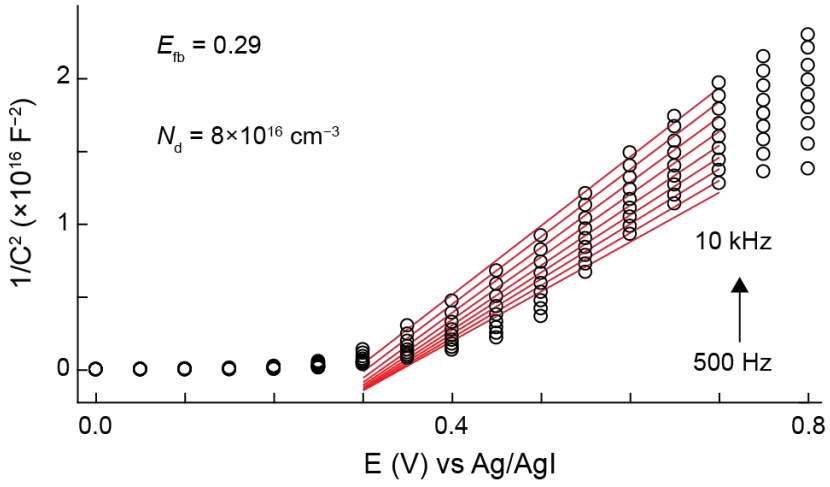

Figure 2.1. Mott-Schottky analysis of bulk $MoSe_2$. Capacitance versus applied potential data as a function of modulation frequency (black circles) for the bulk $MoSe_2$. Linear fits to the data with the Mott-Schottky equation from +0.3 to +0.7 V yielded an onset potential of +0.29 V and a doping density of 8×10^{16} cm^3.

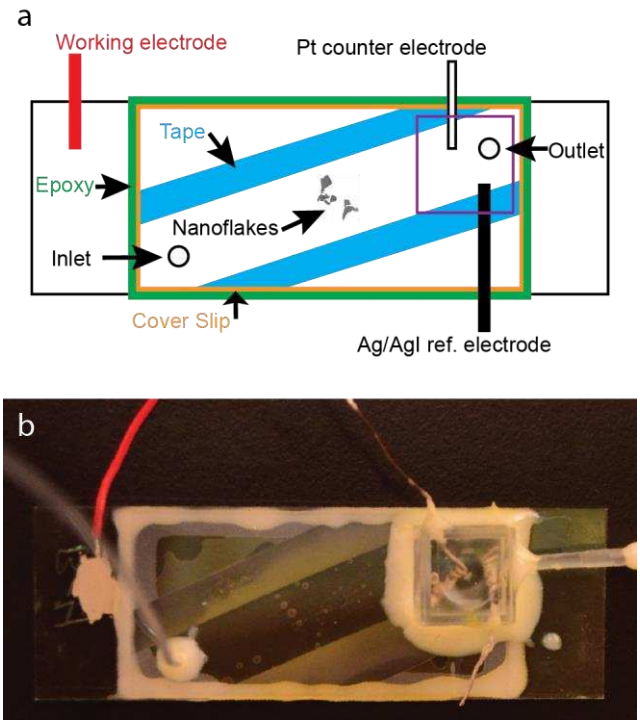

Figure 2.2. Electrochemical flow cell for photocurrent mapping experiments. a) Cartoon illustration of the 3-electrode electrochemical flow cell. The Pt and Ag/AgI electrodes are mounted on the outlet port of the flow cell. b) Photograph of the electrochemical flow cell.

channel. The Ag/AgI reference electrode and Pt counter electrode were placed in the outlet chamber. Electrolyte solution was continuously pulled through the flow cell at a constant rate (50 μL/min, justification provided in main text). The data presented here were measured from a total of 80 nanoflakes (specifically, the photoelectrochemical properties of 18, 3, and 59 nanoflakes were measured from 3 separate electrochemical flow cells).

2.3.3. Photocurrent Mapping and Raman Micro-spectroscopy

Bulk crystal or nanoflake-coated electrochemical flow cells were mounted onto the stage of an inverted optical microscope (Olympus IX73). The experiments were performed in a 500 μm by 500 μm sized region of the ITO electrode. The electrochemical current from the electrode was continuously monitored at 20 Hz for 0.5s at each location

as a focused laser spot was scanned across the sample. A continuous wave 532 nm laser was aligned through the back aperture of either a 10× magnification (UPLFLN10X2) objective for bulk crystal mapping or a 100× magnification (PLFLN100X) objective for nanoflake electrode mapping. The laser spot diameter was 690 nm and 4.94 μm for nanoflake and bulk photocurrent mapping measurements, respectively. The diameter was determined from the full width at half maximum of the beam profile. The power density for nanoflake photocurrent mapping measurements was typically 250 W/cm^2. The laser power density was adjusted to values as high as 2.5 kW/cm^2 in order to achieve signal to noise ratios ≥ 5 for low efficiency nanoflakes (the photocurrent signal was adjusted to be 40 nA and the standard deviation of the electrochemical current was approximately 7 nA as shown in Figure 2.3). The power density for the bulk crystal mapping experiment was 12.5 W/cm^2. Analysis shows that the average error in our EQE measurements is 1.6% (6.5 nA) (Figure 2.3d). Raman spectra were collected from the sample in a backscatter illumination geometry using an Ondax 532 nm THz Raman excitation/detection source.

2.3.4. Scanning Kelvin Probe Microscopy and Auger Micro-spectroscopy of Exfoliated Nanoflakes

Scanning Kelvin probe microscopy measurements were performed under ambient conditions using a single pass mode on a Park AFM (housed in an acoustic box) equipped with an XE-70 controller and an external lock-in amplifier (SR830, Stanford Research Systems). The lock-in amplifier was used for electrical AC bias of the tip, lock-in detection, and feedback at 18kHz of the surface potential signal. Conductive Pt/Ir-coated AFM cantilevers (Multi-75EG, Budget Sensors) were used for the measurements.

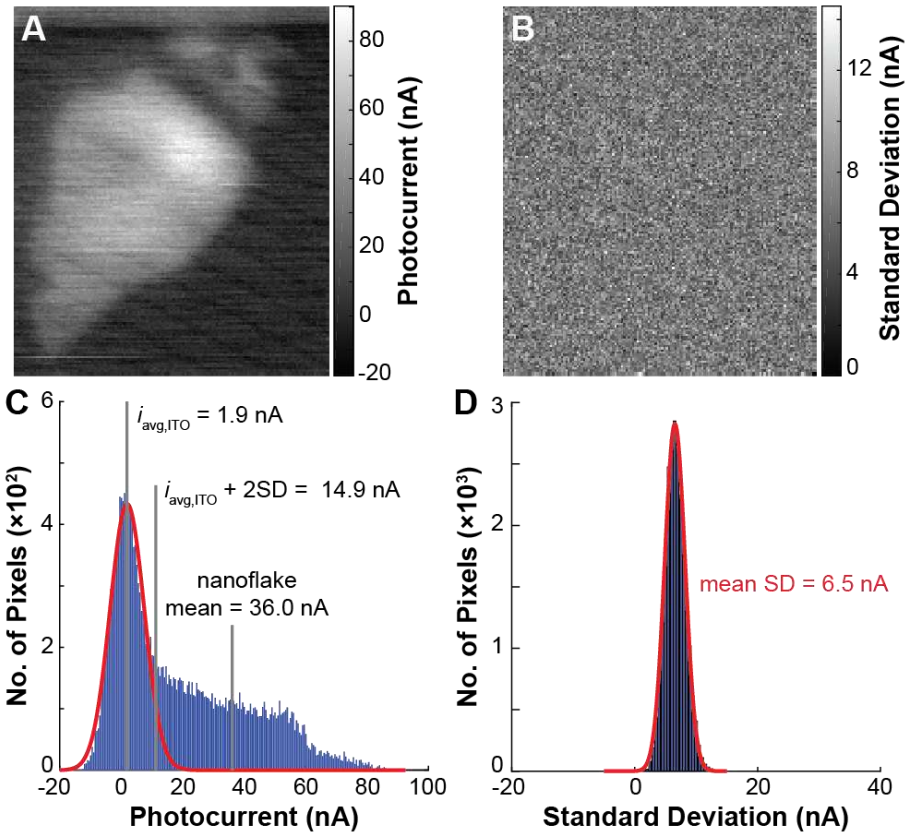

Figure 2.3. Photocurrent map standard deviation analysis. a) Photocurrent map for a nanoflake. b) Standard deviation (SD) of the photocurrent from the same data in (a). c) Distribution of photocurrent values from the nanoflake in (a). The major peak was fit with a Gaussian function (red line) to extract the average background current from the ITO substrate ($i_{avg,ITO}$)= 1.9 nA. The lower limit of detection is defined as $i_{avg,ITO}$ + 2SD = 14.9 nA, where SD is determined in (d). d) Distribution of SD values from panel (b), where the mean SD = 6.5 nA was determined from a Gaussian fit (red line).

Topography was measured at the first resonant frequency (70 kHz) and surface potential was collected with a 1.00 V AC bias at 18 kHz, well separated from the topography frequency. Surface topography and potential were imaged separately. Auger experiments were performed at 10^{-10} Torr on a Phi Electronics 670 Auger nanoprobe.

2.4. Results and Discussion

Figure 2.4a shows the experimental setup, where a nanoflake-coated ITO electrode is assembled into a 3-electrode electrochemical flow cell and mounted on to the

stage of an inverted optical microscope. In a typical experiment, the photocurrent is continuously monitored as a focused laser spot is scanned across the nanoflake-coated

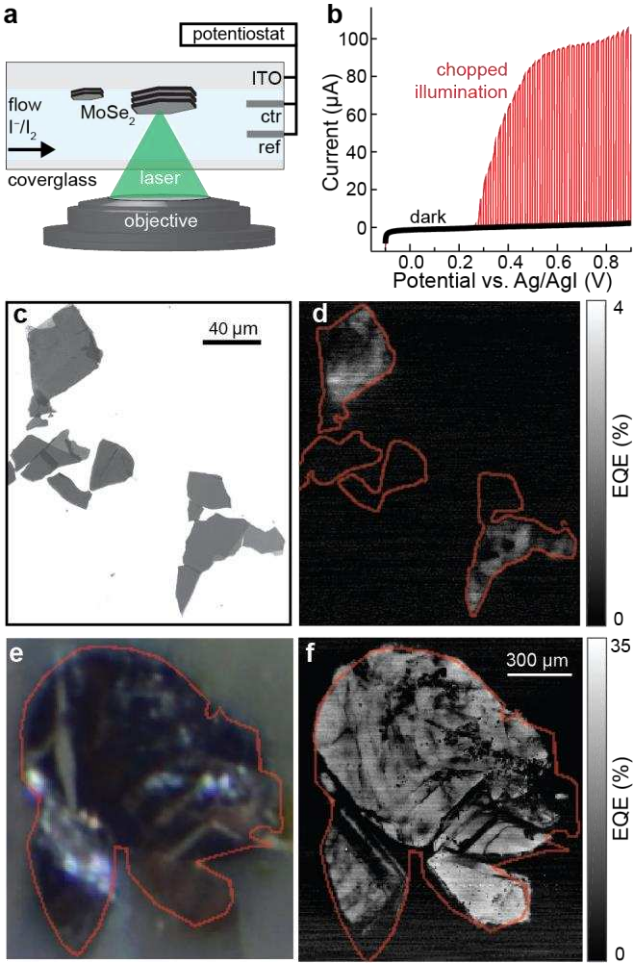

Figure 2.4. Bulk and single-nanoflake photocurrent mapping. a) Experimental setup for single-nanoflake photocurrent mapping in a 3-electrode electrochemical flow cell. The same cell was used for bulk crystal mapping. ctr = Pt wire counter electrode. ref = Ag/AgI wire reference electrode. b) Current-potential curves of a 1.3 mm^2 $MoSe_2$ single crystal in 1 M NaI, 1 mM I_2 electrolyte under dark (black line) and chopped 20 mW/cm^2 532 nm laser illumination (red line). The light spot was larger than the crystal to illuminate the entire electrode surface. c) Bright field optical transmission image of the nanoflake-coated electrode immersed in 1 M NaI, 1 mM I_2. d) EQE map of the nanoflakes in (c) measured at +0.5 V vs. Ag/AgI by scanning a 690 nm diameter 532 nm laser spot in 1 μm increments across the electrode surface. The illumination area and power were 0.37 μm^2 and 3.0 μW, corresponding to a power density of 805 W/cm^2. The red lines represent the nanoflake contour. e) Photograph of the parent bulk $MoSe_2$ crystal used for mechanical exfoliation. f) EQE map of the bulk crystal in (e) measured at +0.5 V with a 4.94 μm diameter 532 nm laser spot in 7 μm increments across the electrode surface. The red line indicates the epoxy contour. The illumination area and power were 19.17 μm^2 and 2.4 μW, corresponding to a power density of 12.5 W/cm^2. The solution flow rate for both mapping experiments was 50 μL/min.

electrode. The spatially localized carrier generation induces a photocurrent response from a single nanoflake, even though there are many other nanoflakes on the same ITO electrode. The photocurrent response stems from photogenerated charge carriers as a function of laser spot position on the nanoflake surface. This approach enables us to probe photocurrent collection efficiency near surface structural features such as interior steps and perimeter edges.

First, we performed ensemble-level photoelectrochemical measurements of bulk $MoSe_2$ | I^-/I_3^- | Pt cells to determine the optimal applied potential for photocurrent mapping measurements. Figure 2.4b shows current-voltage curves of a freshly cleaved bulk n-$MoSe_2$ electrode in 1 M NaI, 1mM I_2 electrolyte under dark and chopped 532 nm laser illumination conditions. Chopped light illumination induced a photocurrent response due to iodide oxidation at potentials more positive than +0.24 V (all potentials are relative to a Ag/AgI reference electrode. The photocurrent increased sharply to a plateau at approximately +0.5 V. All photoelectrochemical microscopy measurements were performed at fixed +0.5 V and under constant electrolyte flow for three reasons. First, the ensemble-average photocurrent increases linearly with light intensity at +0.5 V (Figure 2.5), indicating that the photocurrent is proportional to the number of photogenerated charge carriers within the semiconductor. Because hole transport from the semiconductor interior to the surface does not limit the ensemble-average photocurrent at this potential, the contrast in the photocurrent mapping likely indicates the presence of surface structural features that influence the hole transport efficiency across the semiconductor surface to the electrolyte.[18, 35] Second, electrolyte flow was necessary to maintain steady state photocurrents because it provides high iodide flux to the electrode

and promotes rapid removal of any photogenerated I_2 from the surface (Figure 2.6 and Figure 2.7).[36, 37] Third, the dark current due to electrochemical iodide oxidation[37] should not contribute to electrochemical current because it onsets at +0.7 V (Figure 2.8). Having established an optimal potential for photocurrent mapping, we exfoliated nanoflakes from the bulk crystal using cellophane tape, transferred them onto an ITO electrode according

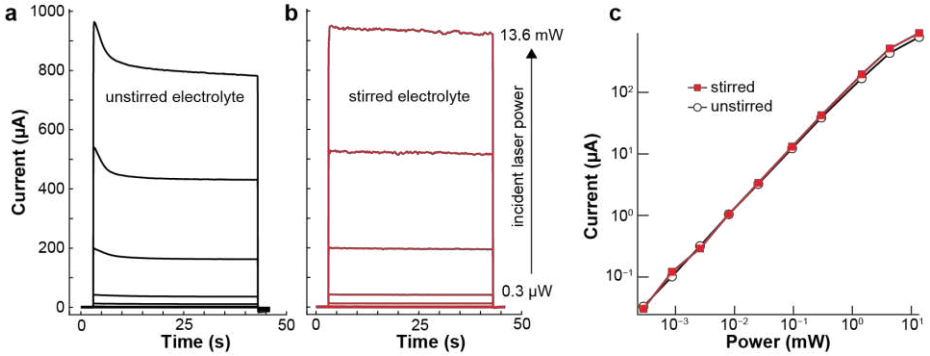

Figure 2.5. Analysis of stirred versus unstirred electrolyte. Ensemble-level photocurrent response of bulk $MoSe_2$ electrodes. a) unstirred, and b) stirred conditions. Initial photocurrent density versus incident 532 nm laser power density for bulk $MoSe_2$ electrodes in a single compartment electrochemical cell under static and vigorous stirring conditions. The data in (c) was calculated from the chronoamperometry data (a-b). The initial photocurrent was determined from the first 500 ms following chopped illumination under b), and c) vigorous stirring conditions. The electrolyte was 0.5 M NaI, 1mM I_2 and applied potential was +0.5 V vs. Ag/AgI. The laser diameter was 2 mm.

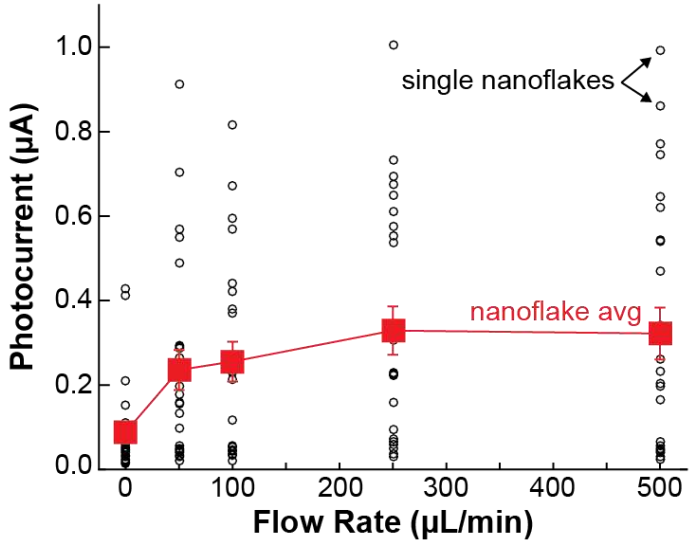

Figure 2.6. Single-nanoflake photocurrent versus solution flow rate. The open black circles represent steady state photocurrent measurements from 25 individual nanoflakes, and the filled red squares represent the averages of these nanoflakes to show the general trend. The electrolyte was 0.5 M NaI, 1mM I_2 at +0.5 V vs. Ag/AgI.

the method described in Huang *et al.*[34], and assembled the 3-electrode flow cell shown in Figure 2.4a. Figure 2.4c shows a representative bright field transmission image of the

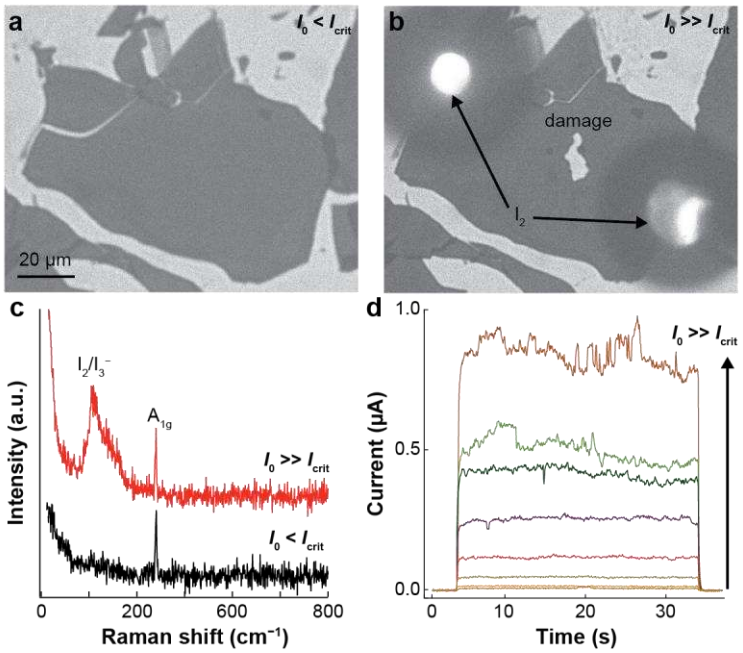

Figure 2.7. *In-situ* optical transmission imaging and Raman micro-spectroscopy of photoexcited nanoflakes. a) Bright field optical transmission image of a single nanoflake a) before and b) after photoelectrochemical measurements at high incident laser power. c) Raman micro-spectroscopy measurements before (black trace) and after (red trace) the formation of surface adsorbed bubble features in (b). d) Current versus time data from chopped illumination experiments as a function of excitation power

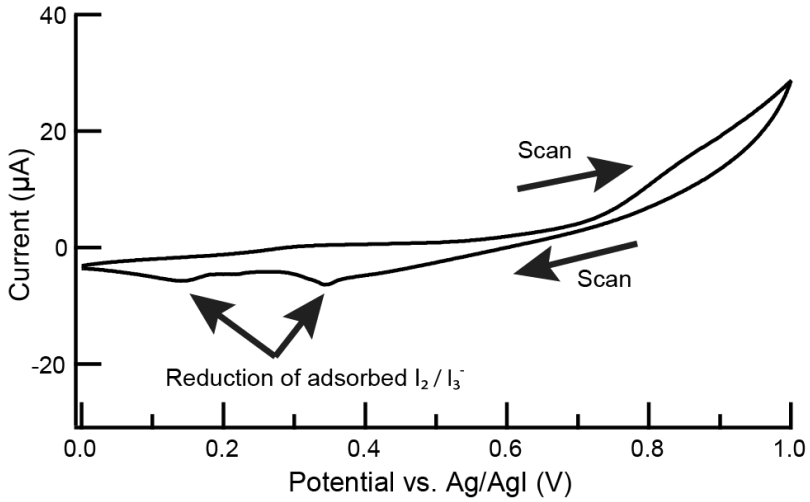

Figure 2.8. Electrochemistry of a bulk $MoSe_2$ electrode in unstirred solution. The black trace shows a cyclic voltammogram under dark conditions. Iodide oxidation onsets at +0.7 V. The potential was scanned from 0.0 V to +1.0 V, and then to 0.0 V at rate of 10 mV/sec.

nanoflake-coated ITO electrode. The exfoliation process produces a heterogeneous distribution of nanoflakes, which motivates our single-nanoflake photoelectrochemical approach to assess their individual photocurrent collection efficiencies. We then scanned a 690 nm diameter 532 nm laser spot in 1 μm increments across the electrode while the steady state photocurrent, i (A), was measured and averaged for 0.5 s at each location. Figure 2.4d shows the resulting EQE map of the sample region shown in Figure 2.4c, where EQE = i/qI_0 and q is the elementary charge and I_0 (photons s^{-1}) is the incident laser power measured at the coverglass. There are significant EQE variations from nanoflake to nanoflake. Additional examples are shown in Figure 2.9. Interestingly, the nanoflakes in Figure 2.4c-d are qualitatively indistinguishable and are separated by only a few microns. The mechanical exfoliation approach allowed us to compare the photoelectrochemical properties of the nanoflake film to the parent bulk crystal. To do so, we assembled the bulk crystal into the same 3-electrode flow cell design as in Figure 2.4a and mounted it onto the stage of the optical microscope. Figure 2.4e shows a

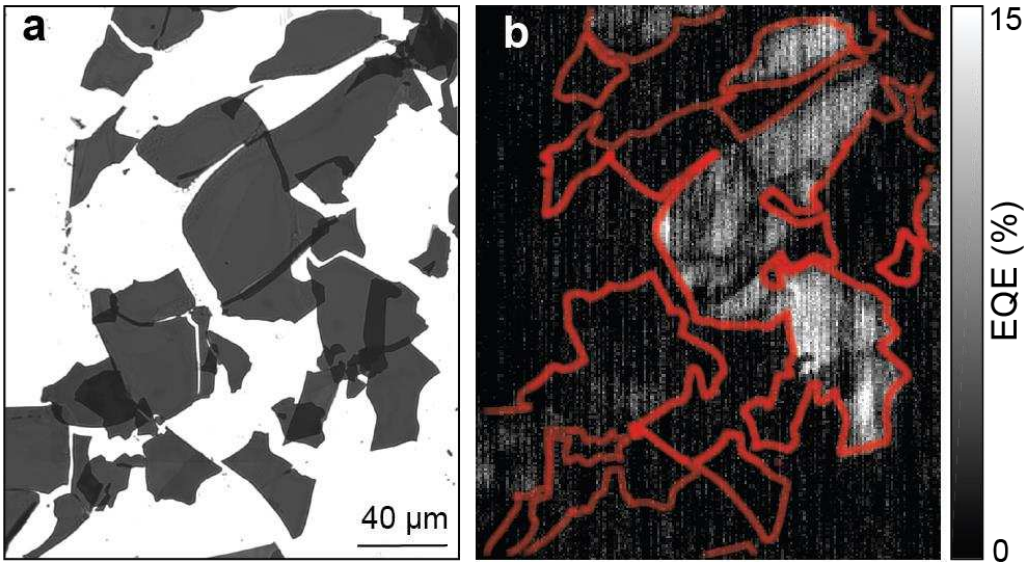

Figure 2.9. Additional example of photocurrent microscopy of exfoliated $MoSe_2$ nanoflakes. a) Bright field optical transmission image and b) corresponding EQE map of the nanoflakes in (a).

photograph of the bulk $MoSe_2$ electrode and Figure 2.4f shows the corresponding EQE map. The maximum EQE values from the bulk crystal were about 35%. The maximum internal quantum efficiency values were estimated to be about 70%, in agreement with Kline *et al.*[24] because the laser reflection at the coverglass and at the crystal surface was measured to be 10% and 34%, respectively. Unfortunately, we are unable to map the photocurrent at higher spatial resolution because the millimeter-thick crystal required a long working distance 10× objective to focus the laser light onto the sample surface, yielding a 15.7 μm^2 illumination area. For example, Figure 2.10 shows that the spatial resolution was not sufficient to reliably determine the photocurrent collection efficiency near smooth and highly stepped regions. Therefore, we focus on comparing the EQE heterogeneity of the entire bulk crystal to that of all measured nanoflakes.

Having obtained photocurrent maps of many individual nanoflakes and their parent bulk crystal, we quantitatively compared the EQE heterogeneity among all illuminated

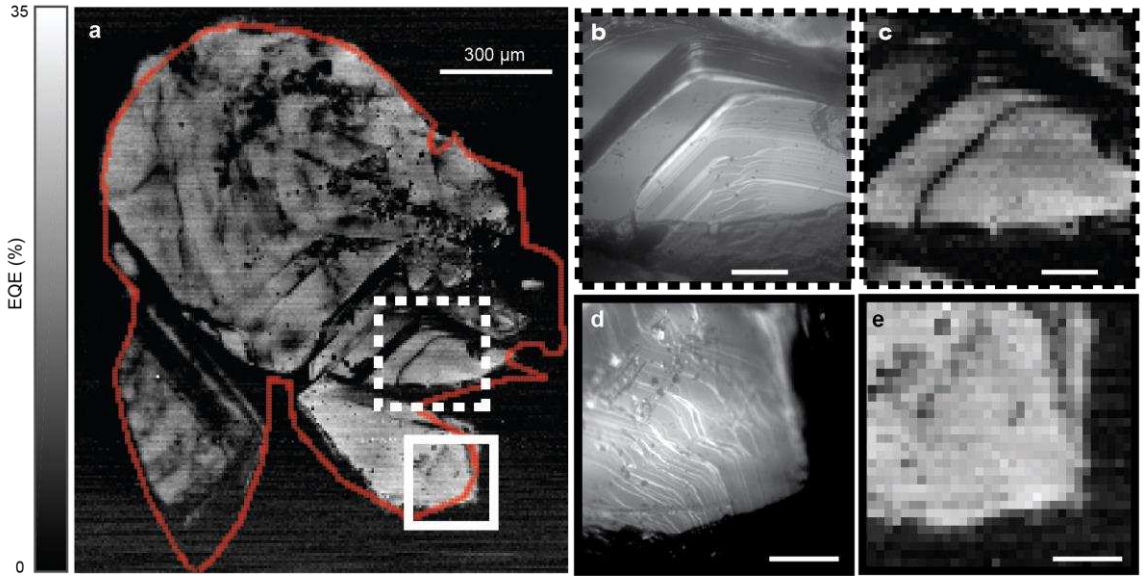

Figure 2.10. Photocurrent microscopy of the bulk $MoSe_2$ crystal in Figure 2.4. a) Complete EQE map of the bulk crystal electrode. b) Optical reflection image and c) the corresponding EQE map of the crystal region in (a) that is indicated by a dashed line box. d) Optical reflection image and corresponding EQE map e) of the region in (a) that is indicated by a solid box. All scale bars in b-e represent 60 μm.

areas of both samples. Figure 2.11a plots the distribution of illuminated surface areas versus their EQE for the bulk crystal (grey bars) and 59 nanoflakes (red squares). Their EQE distributions were normalized to account for differences in laser illumination area and total sample area (Figure 2.12). The bulk crystal EQE distribution shows two major populations: 55% of all illuminated areas produce high EQE values (18 ± 8% EQE) and another 45% of all illuminated areas produce low EQE values (5 ± 5% EQE). The major

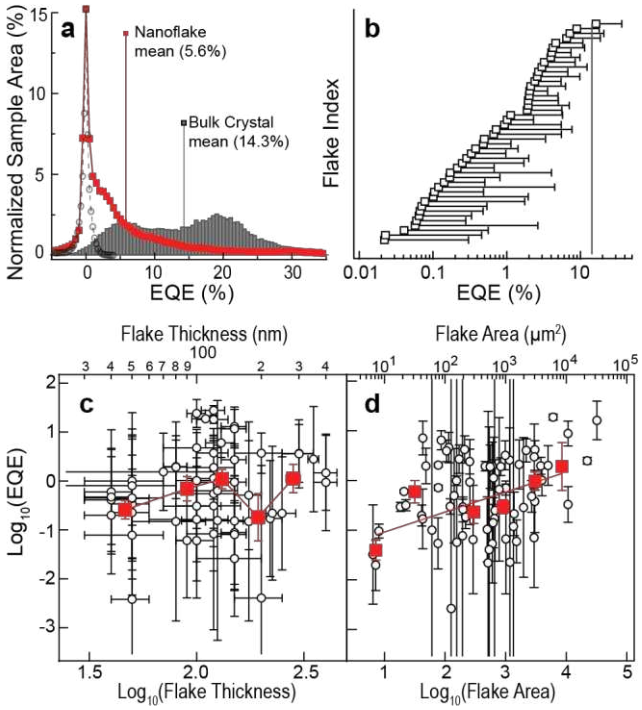

Figure 2.11. Quantitative comparison of bulk and nanoflake photoelectrodes. a) Normalized distributions of all illuminated bulk crystal (grey bars) and nanoflake areas (red squares) versus the EQE values that they produce. The vertical bars represent the mean value for each sample. The black circles represent bare ITO regions. b) Distribution of single-nanoflake mean EQEs (open black squares) compared to the bulk crystal mean EQE (grey vertical line). The error bars represent the upper bound of the 95% credibility region from all EQE values in a single-nanoflake photocurrent map. The data is sorted by EQE and sorted by flake index (arb. units). c) EQE versus nanoflake thickness determined via AFM. EQE values were measured from multiple areas (> 5) of 18 individual nanoflakes. The EQE error bars represent the standard deviation of the EQE sample for 0.5 s and the flake thickness error bars represent the standard deviation of multiple AFM line scans along a nanoflake edge. The red squares represent binned and averaged values to show the general trend, and the error bars represent the standard error of the mean within each bin. d) Mean nanoflake EQE versus nanoflake surface area (open circles). The red squares represent binned and averaged values to show the general trend, and the error bars represent the standard error of the mean.

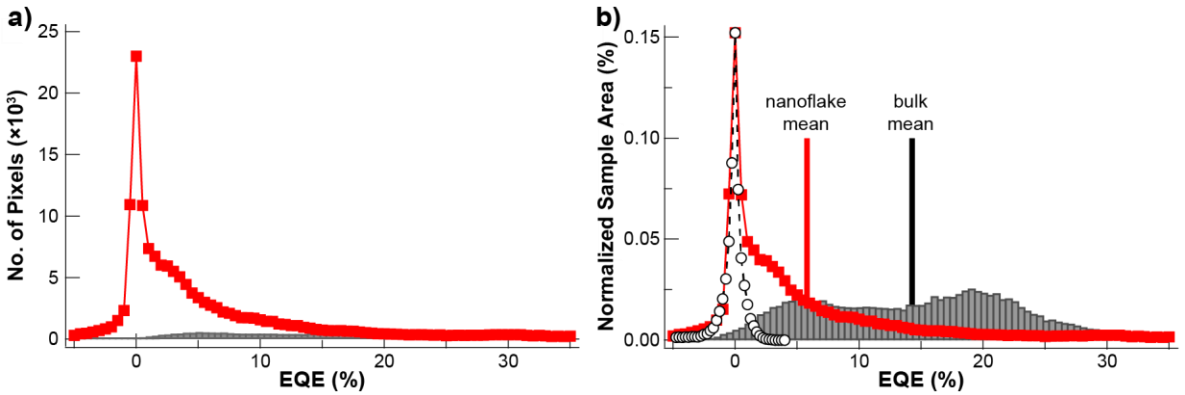

Figure 2.12. Area normalization procedure for nanoflake and bulk EQE distributions. a) EQE distributions of nanoflakes (red squares) and bulk $MoSe_2$ (grey bars). b) Distributions in (a) were multiplied by the following factor: pixel area (μm^2) /total sample area (μm^2), where the pixel area in nanoflake and bulk photocurrent mapping experiments was 1 μm^2 and 49 μm^2, respectively.

difference between the bulk and nanoflake EQE distributions is that 40% of all illuminated nanoflakes produce EQE values equal to that of ITO areas (<1.5% EQE, see black circles in Figure 2.11a). The remaining 60% al all illuminated nanoflake areas produce EQE values that extend to the highest EQE values measured from the bulk crystal. This observation shows that illuminated nanoflake areas can generate photocurrents that are equal to the parent bulk crystal. Furthermore, the distinct components in the EQE distributions suggests that the wide variation in energy conversion properties of the nanoflake sample stems from the exfoliation and transfer process rather than the inherent inhomogeneity of the bulk crystal. For the latter situation, the nanoflake EQE distribution would be expected to reflect the parent sample EQE distribution, but we observed a narrower nanoflake EQE distribution with unique components.

We computed mean EQE values from the nanoflake and bulk crystal photocurrent mapping experiments because they represent the expected EQE values that are typically measured under macroscopic illumination in ensemble-average measurements. The vertical bars in Figure 2.11a at 14.3% and 5.8% indicate a mean EQE of the entire bulk

crystal and all 59 nanoflakes, respectively. The mean EQE of the nanoflake-coated electrode is lower than the bulk crystal, in agreement with Sivula and co-workers.[10] Our photocurrent microscopy experiments reveal that the average photocurrent efficiency of the nanoflake electrode is lower than that of the bulk because the nanoflakes have a much higher fraction of inactive areas (<1.5% EQE) and a much lower fraction of active areas (>10% EQE). We then explored how variations among nanoflakes contribute to the overall lower EQE.

To gain deeper insight into the ensemble-average differences between bulk and nanoflake films, we investigated EQE distributions at the single-nanoflake level. Figure 2.11b shows single-nanoflake mean EQE values and the upper bound of their 95% credibility region (an example of the 95% credibility region for a single nanoflake is shown in Figure 2.13). The credibility regions indicate that at least 95% of all measured values from a single nanoflake lie within the upper and lower bounds (not shown for clarity) of the credibility regions. Interestingly, >10% of illuminated areas on 4/59, or 7%, of these

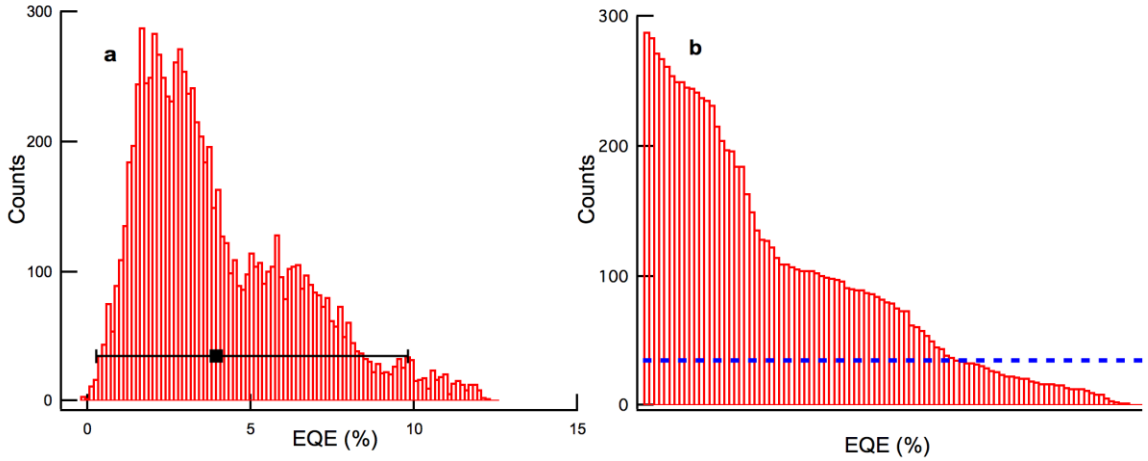

Figure 2.13. Determination of the 95% confidence interval for individual nanoflakes. a) EQE pixel distribution for an active flake. The black square represents the mean value and the credibility region determined from (b). b) Histogram in (a) sorted by bin counts or occurrences. The blue dashed line represents the bin counts that contain 95% of the data; only those bins which extend above the blue dashed line are contained within the credibility region.

nanoflakes produce EQE values that exceed the bulk crystal mean. This “champion” population, which is hidden in ensemble-average measurements, reveals that some isolated nanoflakes can achieve similar photocurrent efficiencies to bulk single crystals. The second major observation form Figure 2.11b is that there is a large population of “spectator” nanoflake population (40/59, or 68% of nanoflakes) whose mean EQE values are equal to bare ITO regions. These spectator nanoflakes are detrimental to device performance because they absorb a significant fraction of incident photons, but they do not produce photocurrent. We note that these inactive flakes are electrically connected to the ITO substrate because they produce a measurable steady state photocurrent under much higher illumination intensities (e.g., >10 kW/cm^2), but the resulting EQE values are <1.5%. The spectator population is mostly responsible for the poor performance compared to the bulk crystal.

One explanation for the spectator nanoflakes is that there is a large contact resistance at the $MoSe_2$/ITO interface. These nanoflakes were deposited directly onto the bulk ITO substrate whereas In/Ga eutectic was used to make an ohmic contact at the bulk $MoSe_2$/ITO interface. While it is known that the electrical properties at the back contact can impact bulk TMD photoelectrochemical cells[38], it is unclear to what extent the back contact impacts the photocurrent response of nanoflake-coated electrodes. Large, variable contact resistances from nanoflake to nanoflake could be a general issue for exfoliated TMDs that are transferred to ITO substrates. For example, liquid exfoliated nanoflake samples are also deposited directly on to ITO substrates because it is technically challenging to apply the In/Ga eutectic beneath individual nanoflakes. Regardless of the exact origin of the spectator population, the champion population

shows that it is possible to achieve highly efficiency charge carrier extraction at direct $MoSe_2$/ITO interfaces.

ITO variations among nanoflakes are not due to differences in light absorption. We performed a 1:1 photocurrent microscopy : atomic force microscopy (AFM) study and determined that the EQE is independent of nanoflake thickness over the broad range of 40 – 400 nm (Figure 2.11c). This can be rationalized by the fact that all these nanoflakes are so-called “optically thick”, meaning that they absorb a significant fraction of charge carriers within their estimated 50 nm-thick depletion region, and the photocurrent is proportional to charge carriers generated within the depletion region. While the EQE is independent of nanoflake thickness, we observed a strong, positive correlation between EQE and nanoflake area; Figure 2.11d shows that large area nanoflakes produce high EQE values. The positive correlation between EQE and nanoflake area suggests that perimeter edge sites impact the photocurrent response, as the number of perimeter edge sites is strongly correlated with nanoflake area (Figure 2.14).

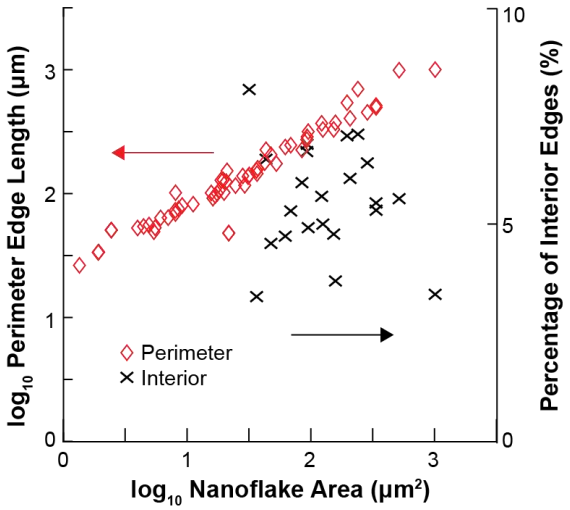

Figure 2.14. Correlation of nanoflake area and edge site quantity. Perimeter edge length (red diamonds) and percentage of nanoflake area that are interior edge sites (black x symbols) versus nanoflake area. The number of edge sites is directly proportional to nanoflake area, while interior edge sites are not.

To explore the impact of perimeter edge sites on photocurrent collection efficiency, we examined the EQE versus illumination distance to the nearest edge site (*r* in Figure 2.15b). Perimeter edges are indicated by red in Figure 2.15b. Figure 2.15c shows that the EQE increases with *r* for the nanoflake shown in Figure 2.15a-b. This trend, which holds for 22/59 (37%) nanoflakes (Figure 2.16 and Figure 2.17), corresponding to the active population of nanoflakes, indicates that photogenerated electrons near perimeter edges are not extracted at the $MoSe_2$/ITO contact. Thus, these perimeter edges are

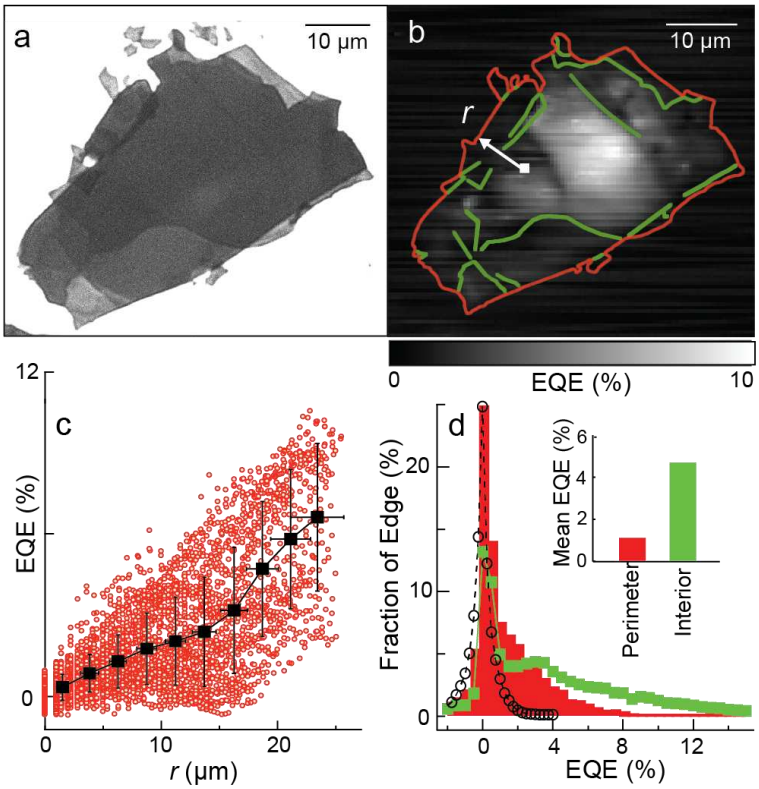

Figure 2.15. Imaging charge carrier generation and recombination at perimeter and interior steps. a) Bright field transmission image of a single nanoflake. b) EQE map for the nanoflake in (a). The red and green pixels represent perimeter edges and interior steps, respectively. The vector *r* represents the distance from a pixel in the EQE map to the nearest perimeter edge. c) Plot of EQE versus *r* for the nanoflake in (a). The small red circles represent data from every pixel within the nanoflake contour and the large black squares represent binned and averaged values to show the general trend. The error bars represent the standard deviation within each bin. d) Distribution of all illuminated perimeter edges (red bars) and interior steps (green squares) versus their EQE. The ITO response (black circles) is shown for comparison. Inset shows the average EQE of all perimeter edges versus interior steps.

recombination sites. This observation is in agreement with previous bulk photocurrent mapping studies that showed lower photocurrent collection efficiency near step edge sites than at apparently smooth basal planes.[5, 17, 18, 39-41]

Interestingly, Figure 2.17c shows that the EQE is more sensitive to illumination distance to the nearest perimeter edge than to the nearest interior step edge on the

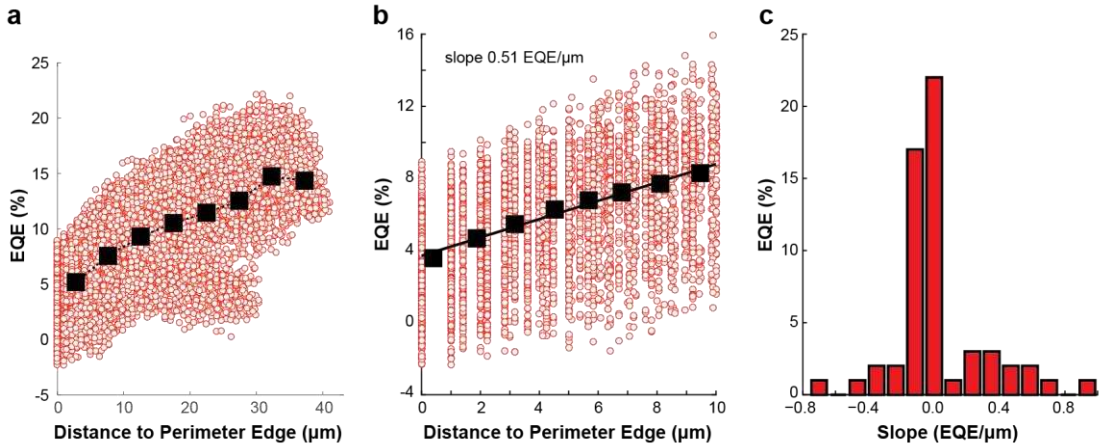

Figure 2.16. Quantifying the percentage of nanoflakes whose EQE increases with distance to perimeter edge (*r*). a) EQE versus distance to perimeter edge (*r*) for the nanoflake shown in Figure 2.15. b) Same data as in (a) over the range $0 \leq r \leq 10$ μm, and the data was fit with a linear function, yielding a slope = 0.51 EQE/μm. c) Distribution of slope values for all 59 nanoflakes in this study. 22 nanoflakes have a positive slope.

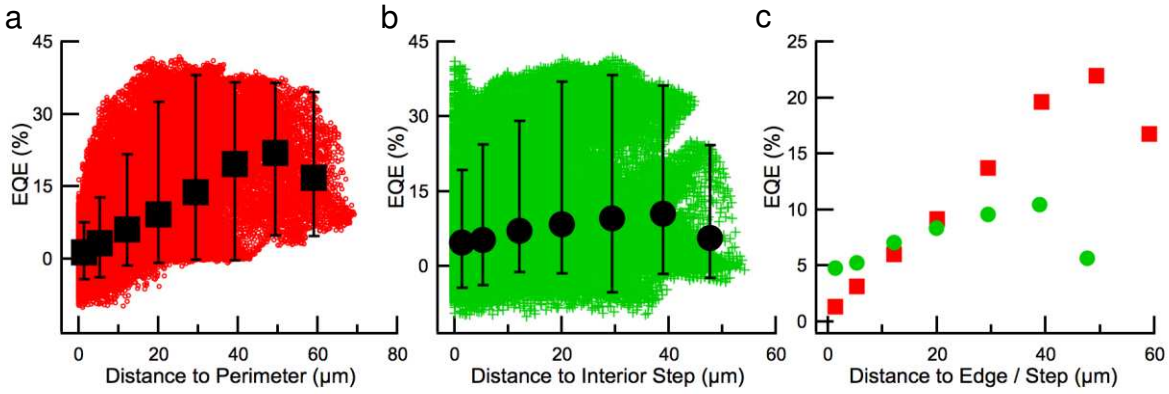

Figure 2.17. EQE versus distance to surface structural features. EQE vs distance to the nearest a) perimeter edge (red points) and b) interior step edges (green crosses) for all illuminated regions of 59 nanoflakes. The large filled symbols in (a) and (b) represent binned and averaged data to show the general trend. The error bars represent the 95% credibility region. c) Comparison of EQE versus distance to either perimeter or interior edges. The red squares represent the binned and averaged data from (a) and the green circles represent the binned and averaged data from (b).

nanoflake surface (interior step edges are indicated by green lines in Figure 2.15b). The origin of the distance dependent sensitivity difference between perimeter and step edge sites is currently unknown, but here we discuss two possible explanations. First, the major distinguishing feature of perimeter edge versus interior edge motifs is the presence of the $MoSe_2$ perimeter site/ITO/electrolyte junction. It is possible that there is rapid exchange of electrons at this junction that leads to increased charge carrier recombination and the EQE versus *r* behavior in Figure 2.15c. Second, Lewerenz *et al.*[17] proposed that, for bulk crystals, 1) electric fields form at step edges and they extend in the parallel direction to the $MoSe_2$ layers and 2) charge carriers are preferentially transported along these electric fields to edge sites because the minority carrier mobility is greater parallel to the layers than perpendicular to the layers. For these exfoliated nanoflakes, the perimeter edge height (40-500 nm in Figure 2.11c) is generally much greater than the step height (10 nm in Figure 2.18a), and therefore it is possible that the electric field strength parallel to the $MoSe_2$ layers is greater at perimeter edges than interior step edges. Thus, the EQE is less sensitive to *r* for interior step edges because charge carriers

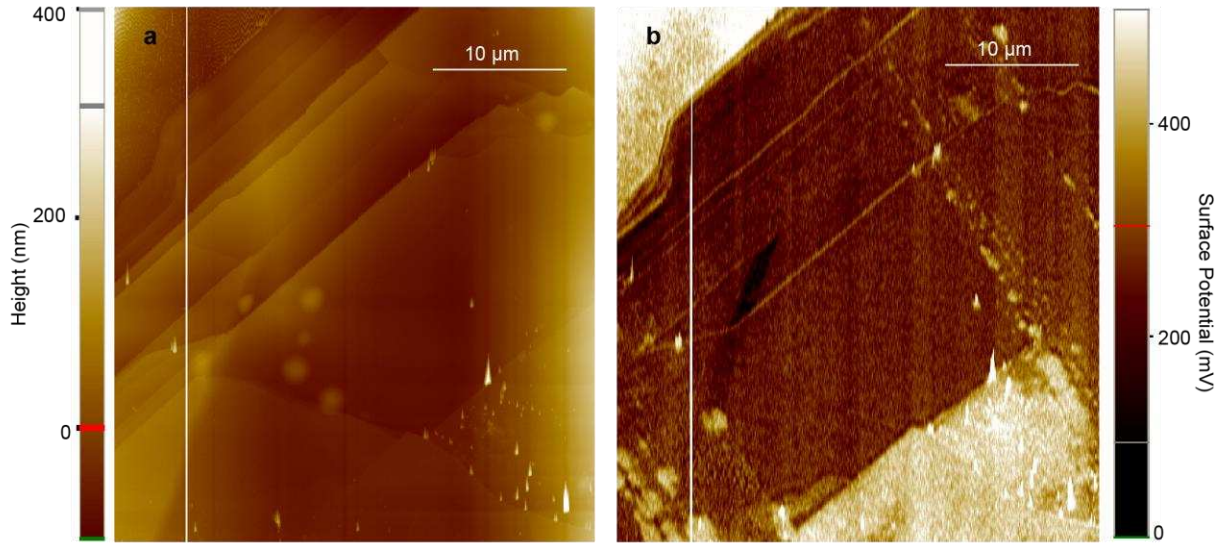

Figure 2.18. Nanoflake Step Characterization. a) AFM topography and b) Kelvin Probe microscopy of an exfoliated $MoSe_2$ nanoflake surface in air.

are preferentially transported to the top surface of the nanoflake, rather than towards deleterious step edges. However, these exfoliated nanoflakes exhibited significant photocurrent efficiency losses up to 10 μm from a perimeter edge despite the fact the space charge region thickness at +0.5V is approximately 50 nm. Therefore, it is unlikely that electric field driven transport is the dominant contributor to enhanced perimeter edge site recombination on these nanoflakes.

Next, we discuss how direct illumination of perimeter and interior step edges impacts the photocurrent collection efficiency, Figure 2.15d shows the distribution of EQE values measured from all illuminated interior steps and perimeter edges from all 59 nanoflakes. Both interior steps and perimeter edges exhibit inactive populations that are equivalent to the ITO substrate (<1.5% EQE). However, the interior steps produce a larger fraction of high EQE values and a lower fraction of low EQE values. As a result, on average, illuminated interior steps produce larger photocurrents than illuminated perimeter edges (Figure 2.15d inset). AFM and Kelvin probe microscopy measurements of these nanoflake samples in air showed that the surface potential varied abruptly (~ 1 nm) at some interior steps (Figure 2.18b). One explanation for higher photocurrent collection efficiency at interior edge sites is that surface dipoles influence the local band bending and/or increase iodine oxidation catalysis, thereby reducing charge carrier recombination compared to perimeter edges. It is currently unclear why these surface potential variations do not occur at all interior steps and whether the surface potential varies abruptly at perimeter edges.

While charge carrier recombination is, on average, more significant at perimeter sites than at interior sites (Figure 2.15d inset), our photocurrent microscopy experiments

revealed that 4% of illuminated perimeter edges are “hot” edges, or produce an EQE greater than the nanoflake mean (5.6% in Figure 2.15d). In some cases, “hot” perimeter edges produce the highest EQE values within a single nanoflake (Figure 2.19). The chemical and/or physical origin of these “hot” perimeter edges are challenging to

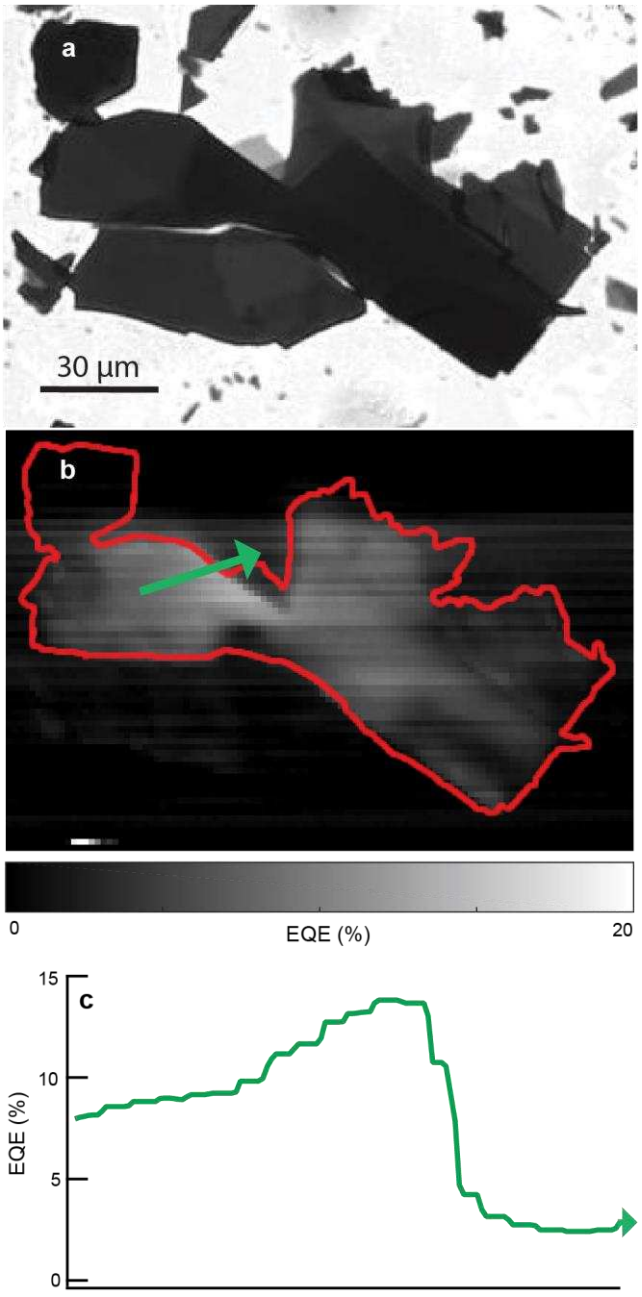

Figure 2.19. Observation of "hot" perimeter edge sites on single nanoflakes. a) Optical transmission image of a single nanoflake and b) corresponding EQE map. c) EQE line profile measured from the solid green line in (b). The green arrow indicates the direction of the line scan. The highest EQE is observed at the nanoflake edge.

determine because it requires atomic-level characterization of the $MoSe_2$ nanoflake edge. Previous bulk crystal photocurrent mapping experiments suggested that “hot” edges are due to preferential adsorption and oxidation of I_3^- at photogenerated Mo(VI) edge sites.[29] Identifying and selectively exposing “hot” perimeter edge sites is critical to achieve high efficiency exfoliated nanoflakes, but is beyond the scope of this work.

Finally, we examined the EQE across apparently smooth basal planes of individual nanoflakes. Figure 2.20a shows an optical transmission image of a single nanoflake and Figure 2.20b-c show how the EQE map was segmented according to the basal plane structure. Figure 2.20d plots the relative standard deviation (RSD) versus the mean EQE for 8 basal planes from the nanoflake in Figure 2.20a (large symbols), as well as for 36

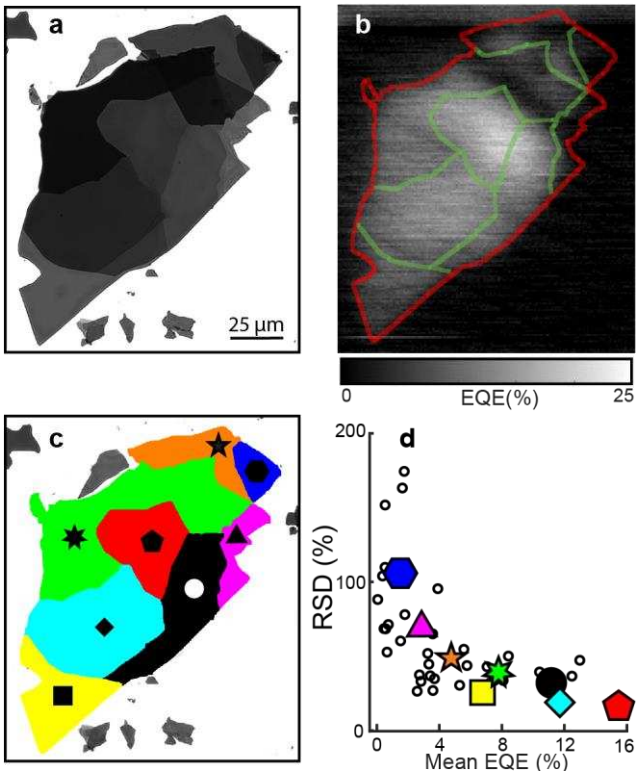

Figure 2.20. Photocurrent heterogeneity across apparently smooth basal planes. a) Transmission image of a nanoflake. b) EQE map of the nanoflake from (a). c) Representation of the nanoflake in (a) in which apparently smooth basal planes are indicated by colors and symbols. d) Relative standard deviation (RSD) versus mean EQE for 44 basal planes measured from 15 nanoflakes. The large symbols indicate data from 8 basal planes in (c).

basal planes from 14 nanoflakes. Figure 2.20d shows that the least active basal planes have the most EQE variation. This trend suggests that the lowest efficiency basal planes have a larger distribution of surface defects or impurities that cause the EQE to vary from location to location across the plane. High resolution Auger mapping (Figure 2.21c-e) showed that adventitious carbon impurities and surface oxygen species were present on basal planes. Figure 2.21b also shows significant carbon content near nanoflakes, presumably due to residual tape residue. Similar features were observed in optical reflection imaging (Figure 2.21f), but the presence of residual tape residue does not impact the photocurrent collection efficiency of the nanoflake (Figure 2.21h), which achieves high EQE values even with the presence of tape residue. It is also possible that Se vacancies contribute to charge carrier recombination across apparently smooth basal planes.[30] The defect states introduced by these surface impurities could account for

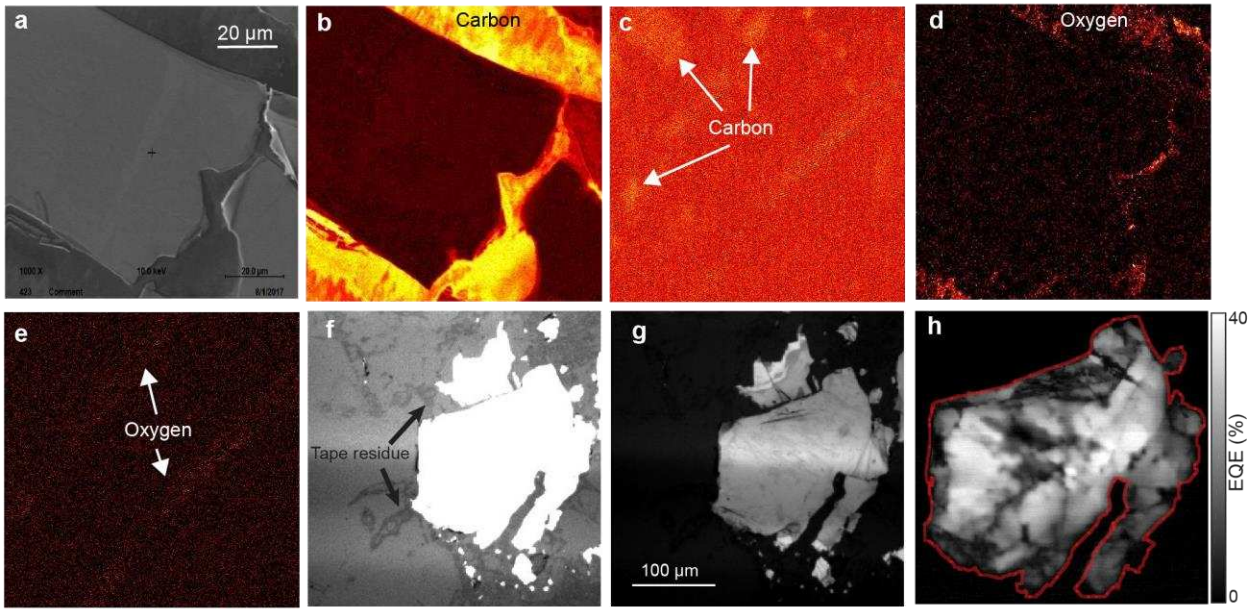

Figure 2.21. Auger compositional analysis of nanoflake areas. a) SEM image of $MoSe_2$ nanoflakes. Elemental maps of b) C, and d) O with Auger micro-spectroscopy. Panels c) and e) represent zoomed-in C and O regions on a basal plane, respectively. (f-g) optical reflection images that are contrasted differently to highlight (f) tape residue on the substrate surface, or (g) surface structure of the $MoSe_2$ nanoflakes. h) EQE map of the nanoflake in (f-g).

spatial variations in interfacial charge transfer kinetics across and among apparently smooth basal planes.

2.5. Conclusions

In conclusion, our single-nanoflake photoelectrochemical measurements revealed that there is a small, high-efficiency “champion” population, as well as a large, low-efficiency “spectator” population within mechanically exfoliated nanoflake thin film electrodes. The observation of champion nanoflakes, which are hidden in ensemble-average measurements, shows that exfoliated 2D semiconductors can be transferred to conducting substrates and retain the excellent energy conversion properties of bulk crystals. However, the spectator nanoflakes, which are also hidden in ensemble-average measurements, dominate the photoelectrochemical response and are mostly responsible for the low photocurrent efficiency compared to bulk single crystals. Photocurrent mapping of individual nanoflakes revealed that charge carrier recombination is greater near perimeter edges than interior steps. The results reported herein shed light on the energy conversion efficiency gap between exfoliated and bulk TMDs. Moreover, our results highlight research opportunities to improve 2D semiconductor thin film photoelectrodes, such as the need for atomic-level compositional and electrical analysis to understand the role of electric fields and surface defects on the photoelectrochemical properties of these ultra-thin semiconducting electrodes.

3. Single-Nanoflake Investigation of Iodine Film Formation on Mechanically Exfoliated $MoSe_2$ Nanoflakes

3.1. Synopsis

Transition metal dichalcogenides (TMDs) such as $MoSe_2$ and WSe_2 are highly efficient photoelectrochemical solar cells in iodide-based electrolytes. However, one aspect that limits their real-world use is that the iodide oxidation products, I_2 and I_3^-, can adsorb on the TMD crystal surface and block further oxidation of iodide, thereby limiting the photocurrent collection efficiency. While this phenomenon has been observed, it is unclear how absorbed I_2/I_3^- products impact the local photoelectrochemical response. Furthermore, it is unclear how the surface reaction kinetics are correlated with the presence of surface structural motifs (e.g. basal planes, perimeter edges, and interior step edges) on TMD nanoflake thin films, which are promising electrode architectures for large-area solar cell applications. Here, we use single-nanoflake photoelectrochemistry to probe how photogenerated I_2/I_3^- products impact the photocurrent collection efficiency and onset potential for 50 spots on 18 nanoflakes. The photogenerated products form on all types of surface motifs, but the products are formed first on the sites with the highest activity for iodide oxidation and the lowest overpotential for iodide oxidation. These observations highlight important design considerations of liquid junction TMD photovoltaics, especially under concentrated solar illumination intensities.

3.2. Introduction

Semiconducting transition metal dichalcogenides (TMDs), MX_2 (M=Mo or W, and X=S, or Se) exhibit solar-to-electrical energy conversion efficiencies up to 17% when used

in a liquid junction photovoltaic cell.[5, 6] In a typical TMD-based liquid junction photovoltaic device, a bulk semiconducting electrode is immersed in an iodide-based electrolyte and illuminated in a two-electrode configuration. The electric field formed at the semiconductor-electrolyte interface effectively separates photogenerated charge carriers within the TMD. The pathways for photogenerated charge carriers are as follows: electrons are extracted to the back contact to power a load in the external circuit while holes oxidize iodide to iodine or triiodide at the TMD-electrolyte interface. These devices are highly efficient and stable because interfacial hole transfer to adsorbed iodide is fast, however one limiting factor is the slow oxidation product dissociation from the electrode surface.[37]

Tributsch and co-workers previously studied $MoSe_2$ | I^-/I_3^- | Pt cells and reported that iodine films formed on the electrode surface at high incident light intensities.[36] The thick insulating iodine films induced current oscillations in the electrochemical signal that ultimately limited the cell efficiency. While these studies clearly demonstrated I_2 film formation, it was difficult to study the initial formation event and how it impacted the local photoelectrochemical response because the 4 mm^2 illumination area in their experiments was about the same size as the bulk electrode (~9-12 mm^2). In addition, there is a growing interest in developing thin film TMD electrodes based on ~10-100 nm thick exfoliated nanoflakes, but it is unclear how product formation on nanoflake basal planes, interior step edges, and perimeter edge sites impact the local photoelectrochemical response. Here, we use a correlated single-nanoflake photoelectrochemical and *in situ* Raman micro-spectroscopy approach to correlate the photocurrent collection efficiency and onset potential with local iodine/tri-iodide product formation.

3.3. Results and Discussion

Figure 3.1a shows a schematic illustration of the experimental setup, where a 3-electrode electrochemical flow cell is mounted on a motorized XYZ stage of an inverted optical microscope. The microscope is designed to perform scanning photoelectrochemical microscopy and Raman micro-spectroscopy experiments. The photocurrent and Raman maps can be quantitatively overlaid to correlate photocurrent efficiency with Raman spectral features. In a typical experiment, a 532 nm laser with a 690 nm diameter illumination area is scanned across the sample surface while the electrochemical current signal or the Raman scattering signal is acquired. This approach enables us to correlate the photocurrent collection efficiency with $MoSe_2$ Raman modes and any surface adsorbed intermediates (e.g., I_2/I_3^-) with near-diffraction-limited spatial resolution.

Figure 3.1b-d shows representative results from a correlated single-nanoflake photocurrent and Raman mapping experiment. Figure 3.1c shows the photocurrent map of the nanoflake shown in Figure 3.1b., where the photocurrent value at each $1 \times 1\ \mu m^2$ pixel was constructed by monitoring the x-component of the lock-in amplifier signal and averaging the signal over the 1 second acquisition time. The spatially localized carrier generation induces a photocurrent response due to iodide oxidation. The photocurrent response stems from photogenerated carriers in a single nanoflake even though there are many other nanoflakes on the same ITO electrode. The photocurrent map shows heterogeneous photocurrent activity across the nanoflake. We recently showed that the photocurrent efficiency increases with illumination distance to the nearest perimeter edge site,[42] and attributed this behavior to enhanced charge carrier recombination at perimeter

edge sites. This study focuses on how photogenerated surface intermediates impact the photocurrent efficiency and the photocurrent onset potential across a single nanoflake.

To probe the impact of photogenerated intermediates on the local photoelectrochemical properties, we acquired Raman spectra at the same conditions

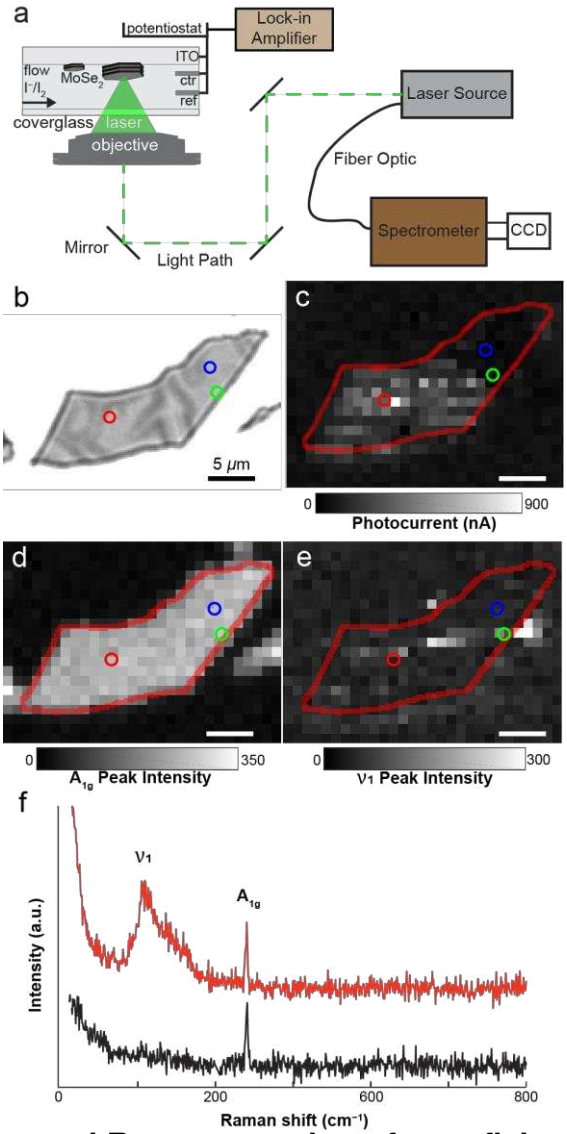

Figure 3.1. Photocurrent and Raman mapping of nanoflakes. a) A schematic of the experimental setup used for mapping experiments. For Raman detection, backscattered light follows the beam path back to the laser source, then gets transferred to the spectrometer via a fiber optic cable. The current signal from the Potentiostat is sent to the Lock-in amplifier. b) An optical transmission image of a nanoflake. The circles indicate different electrochemical investigation sites. c) Photocurrent map of the nanoflake shown in (b). c) $MoSe_2$ A_{1g} Raman peak map of the nanoflake in (b). d) I_2 Raman peak of the nanoflake shown. e) Representative Raman spectra of the A_{1g} peak and I_2/I_3 symmetric stretch, black and red traces, respectively.

used for photocurrent microscopy experiments. Figure 3.1f shows two representative spectra from the nanoflake shown in Figure 3.1a. The peak at 240 cm^{-1} was observed in all spectra and can be attributed to the bulk $MoSe_2$ A_{1g} vibrational mode.[43] In addition, upon illumination of some nanoflake areas, we observed a new major peak at 114 cm^{-1} with a shoulder centered 150 cm^{-1} (Figure 3.1f, top red trace). In some cases, the appearance of these peaks coincided with bubble-like features that were observed in bright field transmission images. Our observations are in general agreement with Tributsch and co-workers' observations that thick I_2 films form on illuminated $MoSe_2$ bulk crystals.[36] Therefore, we assign these Raman peaks to the photogenerated products I_2 and I_3^-. Based on previous *in situ* Raman spectroscopy studies of iodide oxidation on gold electrodes, we assign the 114 cm^{-1} peak to an I_3^- symmetric stretch (ν_1) and the shoulder peak at 150 cm^{-1} to adsorbed I_2.[44, 45]

Next, we examined how the A_{1g} and I_3^- ν_1 modes varied across the nanoflake by fitting these peaks with Lorentzian lineshapes and plotting the peak intensities versus illumination position in Figure 3.1f. We chose to monitor the more prominent I_3^- ν_1 peak at 114 cm^{-1} because its position and intensity could be determined more reliably and the ratios of the two peaks did not change with position. Figure 3.1d shows that the A_{1g} peak intensity is fairly uniform across the surface of the nanoflake. We attribute this to the fact that this a bulk Raman mode and the bright field transmission image does not indicate thickness variations across the nanoflake. The uniformity of the A_{1g} map indicates that the photocurrent variations across the flake are not due to major thickness variations in the material, in agreement with our previous correlated AFM study.[42] However, Figure 3.1e shows the I_3^- ν_1 peak intensity varies significantly from location to location across the

nanoflake. This observation suggests that formation of photogenerated surface adsorbed products begins at specific nanoflake surface sites. The nanoflake in Figure 3.1e shows I_3^- ν_1 formation on the top surface (basal plane) and at the perimeter edge. For the 18 nanoflakes examined in this study, we observed that I_3^- and I_2 formation is not limited to one class of surface structures (e.g. interior step, perimeter edge, basal plane). It is important to note that the Raman measurement probes where I_3^- and I_2 are formed on the surface within the laser illumination spot, whereas the photocurrent measurement reports on charge carrier collection efficiency as a function of carrier generation location (not where the charge carriers react at the surface).

We then studied I_2/I_3^- formation at different locations on individual nanoflakes. We fixed the electrode potential at a high band bending condition (+0.5 V vs. Ag/AgI) and measured the current response as a function of incident light intensity (I_0) from 50 locations across 18 nanoflakes. Measurements were performed on apparently smooth basal planes (blue circle in Figure 3.1a), interior step edges, perimeter edge sites (green circle in Figure 3.1), as well as I_2/I_3^- "hot spots" that were identified in Raman mapping experiments (red circle in Figure 3.1d). We performed measurements at +0.5 V because the photocurrent magnitude was independent of the applied potential for $E > +0.3$ V vs. Ag/AgI.[42] Figure 3.2a shows representative chronoamperometric data under chopped light illumination. We observed that the photocurrent magnitude increased with increasing light intensity. In addition, at the highest incident light intensities, we observed fluctuations in the photocurrent-time response. Tributsch and co-workers also observed photocurrent fluctuations on bulk $MoSe_2$ crystals and attributed the phenomenon to the formation and dissolution of adsorbed iodine.[36] To quantify the magnitude of the photocurrent

oscillations, we computed the derivative of the photocurrent-time response and observed that the d*i*/d*t* distributions were narrow at low light intensity and broad at high light intensity (open circles in Figure 3.2b). We fit the d*i*/d*t* distributions with a Gaussian function (solid lines in Figure 3.2b) and plotted the standard deviation of the Gaussian fit, σ, versus the illumination intensity (Figure 3.2c). The σ parameter, which represents the average current oscillation under illumination, is constant at low light intensity and then increases with incident light intensity. To quantify the critical incident light intensity that induces

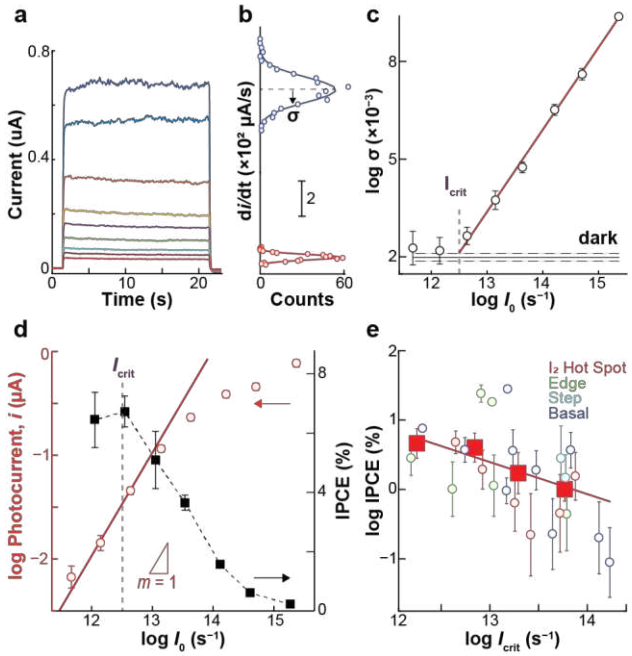

Figure 3.2. Determination of I_{crit} via local chronoamperometry. a) A representative chronoamperometry experiment at a single nanoflake site showing 9 current traces at 9 different illumination intensities. All chronoamperometry measurements were performed at 0.5 V vs Ag/AgI with 30 second laser pulses. b) The distribution of d*i*/d*t* values representing the variation in magnitude of photocurrent oscillations form the traces with the highest a lowest average photocurrent. c) A representative plot of showing the relationship between illumination intensity, I_0, and the first standard deviation, σ, from the Gaussian fits of a d*i*/d*t* plot, as shown in (c). The red line is the linear fit to the data points whose average, including error, are not included by the σ, plus error, from the dark current, shown as solid and dashed black lines, respectively. I_{crit} is the point where the red fit line intersects the upper bound of the error in the d*i*/d*t* of the dark current. d) A plot of I_0 versus photocurrent and IPCE. The vertical dashed line indicates I_{crit} and the solid red line indicates slope = 1. e) A plot of I_{crit} versus IPCE. The red squares represent the binned average of the individual spot measurements. The red line is the linear fit through the binned averages.

photocurrent oscillations (I_{crit}), we fit a line to the σ versus I_0 data in Figure 3.2c and determined the y-intercept equal to $2\sigma_{dark}$ (dashed horizontal black line in Figure 3.2c), where σ_{dark} represents the average current oscillations in the dark. I_{crit} is the minimum illumination intensity where the magnitude of current oscillations under illumination exceeds the magnitude in the dark. Importantly, I_{crit} is the minimum power at which photogenerated products I_2 and I_3^- begin to form on the nanoflake surface.

Having identified the critical power for I_2/I_3^- formation on the nanoflake surface, we then explored how these products impact the photocurrent response. Figure 3.2d shows the average photocurrent under illumination (red circles) versus incident light intensity for the same data in Figure 3.2a. The photocurrent (i) increases linearly with light intensity for $I_0 < \sim 10^{13}$ photons per second (see solid red line in Figure 3.2d), indicating that photogenerated charge carriers can be efficiently extracted from the nanoflake at the high band bending condition. However, for $I_0 > I_{crit}$ the photocurrent no longer increases linearly with light intensity. Moreover, the monochromatic incident photon to current efficiency (IPCE = qi/I_0, where q is the electronic charge) decreases abruptly at I_{crit} (see black squares in Figure 3.2d). Thus, the onset of I_2/I_3^- formation on the nanoflake surface limits the photocurrent collection efficiency. Interestingly, we found a strong negative correlation between the maximum IPCE value of every spot and its I_{crit} (Figure 3.2e). The trend indicates that I_2/I_3^- forms first on illuminated nanoflake spots that have the highest photocurrent collection efficiency. We did not observe any trends between I_{crit} and the surface motifs. In other words, I_2/I_3^- forms on all types of surface motifs and these products are not more likely to form on perimeter or interior edge sites than at basal planes. However, the data suggests that the current collection efficiency varies from

location to location on these nanoflakes because there are local variations in surface reaction kinetics, and the most active sites for iodide oxidation are first to be limited by I_2/I_3^- formation.

While the mechanism by which I_2 decreases the photocurrent is not entirely clear, I_2 films could reduce the photocurrent in two ways. First, I_2 films can reduce light absorption by the nanoflake because they are highly reflective surface coatings, thus decreasing the total number of photogenerated charge carriers.[46] Second, the adsorbed I_2 species forms an insulating barrier layer between the electrolyte and the nanoflake surface. The insulating I_2 layer can reduce the photocurrent by blocking access for solution-phase I^- to reach the electrode surface, thereby preventing interfacial electron transfer and net current flow.

Next we explored how I_2/I_3^- formation impacts the photocurrent onset potential. Linear sweep voltammetry (LSV) experiments were performed under chopped light illumination for 50 spots on 18 nanoflakes. Figure 3.3a shows a representative single-nanoflake LSV measurement from 0.0 V to +0.5 V at a scan rate of 1 mV/sec. The electrochemical current from the ~4 cm^2 nanoflake-coated ITO electrode dominates the total current response, however the modulating photocurrent response due to local chopped illumination can be distinguished from the current in the dark (Figure 3.3a, inset). We then plotted the *i-E* relationship in Figure 3.3b, where *i* was calculated by subtracting the current immediately before illumination (i.e., the dark current) from the current immediately after illumination. It should be noted that *i* is artificially high for $E < 0.1$ due to double layer charging effects and therefore we exclude these data in Figure 3.3b. We extracted the photocurrent onset potential (E_{on}) using a linear fit to the *i-E* data in Figure

3.3b; the *x*-intercept of the linear fit gives E_{on}. Interestingly, we plotted the distribution of E_{on} values for different structural motifs (small square data points in Figure 3.3c) and observed that the average E_{on} depended on the illumination location on the nanoflake (large square symbols in Figure 3.3c). For these nanoflakes, the I_2/I_3^- "hot spots" have the most negative, or most favorable, photocurrent onset potentials. The trend in Figure 3.3c suggests that the sites where I_2/I_3^- is readily deposited require the least driving force or overpotential for the iodide oxidation reaction. There is some indication in Figure 3.3c that the onset potential depends on the type of surface structural motif (i.e., basal plane, interior step edge, or perimeter edge), but the distribution of E_{on} values for different motifs on different nanoflakes is very broad and therefore the average values for the three motifs are about the same. Nonetheless, our data suggests that photogenerated surface adsorbed I_2/I_3^- products initially form on the most catalytically active sites (Figure 3.2e)

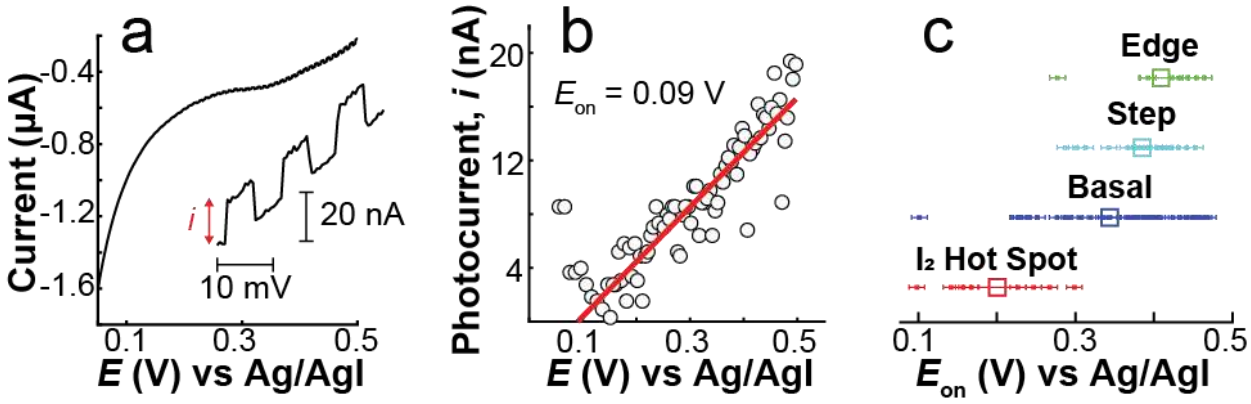

Figure 3.3. Determination of E_{on}. a) A representative LSV of a single measurement site at a fixed laser power. The laser spot was chopped to better resolve the difference between light and dark currents. The inset shows a zoom-in on three pulses of the LSV to show the square waveform of the photocurrent, *i*. The photocurrent is defined as the difference between the light and dark currents. b) A plot of applied potential, *E*, versus *i*. A linear fit was applied to the data points, shown in red. The x-intercept gives the onset potential, E_{on}, of photocurrent from the LSV in (a). It should be noted that the calculated value of *i* is artificially high at potentials less than 0.1 V because of the steepness of the curve in the LSV at lower potentials. c) The distribution of E_{on} values of the different types of sites. The large squares represent the average of the individual data points.

and the most thermodynamically favorable sites that require the lowest overpotential to drive the iodide oxidation reaction (Figure 3.3c).

3.4. Conclusion

$MoSe_2$ thin film $|I^-/I_3^-|$ Pt electrochemical cells are promising for solar-to-electrical energy conversion. However, photo-oxidation products I_2 and I_3^- can adsorb on the $MoSe_2$ surface and limit the cell efficiency. We performed correlated scanning photoelectrochemical microscopy and Raman micro-spectroscopy measurements on single $MoSe_2$ nanoflakes and determined how I_2/I_3^- formation influences the local photoelectrochemical response. We observed that I_2/I_3^- products form on all types of surface structural motifs (basal planes, step edges, and perimeter edge sites), but surface adsorbed I_2/I_3^- products form preferentially on the most active sites for iodide photo-oxidation. In addition, I_2/I_3^- formation is most likely to occur on surface sites that have the lowest onset potential for iodide oxidation. These findings indicate that the most catalytically active and the most thermodynamically favorable sites for iodide oxidation will be most affected under high light intensity conditions, such as solar cell operation under concentrated solar illumination conditions.

4. Outlook

Ultra-thin transition metal dichalcogenides have the potential to be integral to the development of high-efficiency, low-cost, and large-area solar energy-to-electricity applications. Unfortunately, the easily achievable high efficiency of the bulk crystals has not transferred to two-dimensional TMDs. A potential solution to improve the performance of TMD nanoflake based devices, is to reduce the amount of charge carrier recombination in thin films. It is well known that defect sites are highly detrimental to energy conversion processes in these materials. Perimeter edges introduce a high density of unsaturated transition metal and chalcogen atoms at the termination of the crystal structure. These dangling bonds introduce mid-band gap energy levels that can trap photogenerated charge carriers, which then recombine. Defect passivation is a way to decrease the number of defect sites, thus decreasing the deleterious effects of dangling bonds.

Here, passivation means protecting certain surfaces from participating in chemical reactions. There are several approaches to passivate defect sites on semiconductor TMD surfaces. One way is to form bonds at unsaturated atom sites, thus removing the trap state from the dangling bond, passivating the defect, and deceasing recombination. In liquid junction photovoltaic devices, this result can be achieved by physically blocking the defect site with a deposited material. This forms a barrier between the defect site and the electrolyte and prevents the back reaction of electrolyte species. In n-$MoSe_2$ photoelectrochemical cells, this back reaction is the reduction of I_2 or I_3^- and reduces the conversion efficiency of these solar cells.[47, 48]

Canfield and co-workers used pyridine-based molecules in iodide electrolyte to temporarily improve the power output from bulk $MoSe_2$ and WSe_2 electrodes.[47] White *et al.* achieved decreased dark currents and up to 100% power efficiency improvements of bulk WSe_2 electrodes in iodide electrolyte, as well as 300% improvement in power efficiency from WSe_2 | $Fe(CN)_6^{4-/3-}$ | Pt photoelectrochemical cells, by anodic electropolymerization of o-phenylenediamine at defect sites.[48]

While these strategies did lead to improvements in photoelectrochemical cell performance of TMD bulk crystals, the effect of these types of chemical treatments on nanoflake-coated electrodes are not known. As such, it would be worthwhile to use single-nanoflake photoelectrochemical measurements to understand how the charge collection efficiency of a nanoflake changes after defect passivation. This investigation could be achieved by mapping nanoflake photocurrent efficiency before and after chemical treatments. This investigation could also be performed on TMD nanoflakes with defects passivated via covalent functionalization or defect repair.[49, 50] It is possible that, while these chemical treatments have immediate effects on the defect site, significant changes also happen to the photocurrent activities of areas across the surface of a nanoflake. For example, passivating defects at edge sites my increase the number of photoelectrochemically active edge sites, it may also increase the photocurrent activity across the nanoflake as a whole. With this in mind, these spatially resolved photocurrent mapping experiments may provide further insight in to structure-performance relationships of chemically treated two dimensional TMDs.

5. References

1. Velicky, M.; Toth, P. S., From two-dimensional materials to their heterostructures: An electrochemist's perspective. *Applied Materials Today* **2017,** *8*, 68-103.

2. Mak, K. F.; Lee, C.; Hone, J.; Shan, J.; Heinz, T. F., Atomically Thin MoS_2: A New Direct-Gap Semiconductor. *Phys. Rev. Lett.* **2010,** *105* (13).

3. Wang, Q. H.; Kalantar-Zadeh, K.; Kis, A.; Coleman, J. N.; Strano, M. S., Electronics and optoelectronics of two-dimensional transition metal dichalcogenides. *Nat. Nanotechnol.* **2012,** *7* (11), 699-712.

4. Mattheis.Lf, Band Structures of Transition-Metal-Dichalcogenide Layer Compounds. *Phys. Rev. B* **1973,** *8* (8), 3719-3740.

5. Tenne, R.; Wold, A., Passivation of Recombination Centers in n-WSe_2 Yields High-Efficiency (Greater-than-14-Percent) Photoelectrochemical Cell. *Appl. Phys. Lett.* **1985,** *47* (7), 707-709.

6. Prasad, G.; Srivastava, O. N., The High-Efficiency (17.1-Percent) WSe_2 Photo-Electrochemical Solar-Cell. *J. Phys. D: Appl. Phys.* **1988,** *21* (6), 1028-1030.

7. Velicky, M.; Bissett, M. A.; Woods, C. R.; Toth, P. S.; Georgiou, T.; Kinloch, I. A.; Novoselov, K. S.; Dryfe, R. A. W., Photoelectrochemistry of Pristine Mono- and Few-Layer MoS2. *Nano Lett.* **2016,** *16* (3), 2023-2032.

8. Li, H.; Wu, J. M. T.; Yin, Z. Y.; Zhang, H., Preparation and Applications of Mechanically Exfoliated Single-Layer and Multi layer MoS_2 and WSe_2 Nanosheets. *Acc. Chem. Res.* **2014,** *47* (4), 1067-1075.

9. Eng, A. Y. S.; Ambrosi, A.; Sofer, Z.; Simek, P.; Pumera, M., Electrochemistry of Transition Metal Dichalcogenides: Strong Dependence on the Metal-to-Chalcogen Composition and Exfoliation Method. *ACS Nano* **2014,** *8* (12), 12185-12198.

10. Yu, X. Y.; Prevot, M. S.; Guijarro, N.; Sivula, K., Self-assembled 2D WSe_2 thin films for photoelectrochemical hydrogen production. *Nat. Commun.* **2015,** *6*.

11. Nguyen, T. P.; Choi, S.; Jeon, J. M.; Kwon, K. C.; Jang, H. W.; Kim, S. Y., Transition Metal Disulfide Nanosheets Synthesized by Facile Sonication Method for the Hydrogen Evolution Reaction. *J. Phys. Chem. C* **2016,** *120* (7), 3929-3935.

12. Backes, C.; Higgins, T. M.; Kelly, A.; Boland, C.; Harvey, A.; Hanlon, D.; Coleman, J. N., Guidelines for Exfoliation, Characterization and Processing of Layered Materials Produced by Liquid Exfoliation. *Chem. Mater.* **2017,** *29* (1), 243-255.

13. Py, M. A.; Haering, R. R., Structural Destabilization Induced By Lithium Intercalation in MoS_2 snd Related-Compounds. *Can. J. Phys.* **1983,** *61* (1), 76-84.

14. Voiry, D.; Salehi, M.; Silva, R.; Fujita, T.; Chen, M. W.; Asefa, T.; Shenoy, V. B.; Eda, G.; Chhowalla, M., Conducting MoS_2 Nanosheets as Catalysts for Hydrogen Evolution Reaction. *Nano Lett.* **2013,** *13* (12), 6222-6227.

15. Fan, F. R. F.; White, H. S.; Wheeler, B.; Bard, A. J., Semiconductor Electrodes .29. High-Efficiency Photoelectrochemical Solar-Cells with n-WSe_2 Electrodes in an Aqueous Iodide Medium. *J. Electrochem. Soc.* **1980,** *127* (2), 518-520.

16. Gobrecht, J.; Tributsch, H.; Gerischer, H., Performance Of Synthetical n-$Mose_2$ In Electrochemical Solar-Cells. *J. Electrochem. Soc.* **1978,** *125* (12), 2085-2086.

17. Lewerenz, H. J.; Heller, A.; Disalvo, F. J., Relationship Between Surface-Morphology and Solar Conversion Efficiency of WSe_2 Photoanodes. *J. Am. Chem. Soc.* **1980,** *102* (6), 1877-1880.

18. Parkinson, B. A.; Furtak, T. E.; Canfield, D.; Kam, K. K.; Kline, G., Evaluation and Reduction of Efficiency Losses at Tungsten Diselenide Photoanodes. *Faraday Discuss.* **1980,** *70*, 233-245.

19. Levyclement, C.; Heller, A.; Bonner, W. A.; Parkinson, B. A., Spontaneous Photoelectrolysis of HBr and HI. *J. Electrochem. Soc.* **1982,** *129* (8), 1701-1705.

20. Baglio, J. A.; Calabrese, G. S.; Harrison, D. J.; Kamieniecki, E.; Ricco, A. J.; Wrighton, M. S.; Zoski, G. D., Electrochemical Characterization of Para-Type Semiconducting Tungsten Disulfide Photo-Cathodes - Efficient Photo-Reduction Processes at Semiconductor Liquid Electrolyte Interfaces. *J. Am. Chem. Soc.* **1983,** *105* (8), 2246-2256.

21. Sobczynski, A.; Yildiz, A.; Bard, A. J.; Campion, A.; Fox, M. A.; Mallouk, T.; Webber, S. E.; White, J. M., Tungsten Disulfide - A Novel Hydrogen Evolution Catalyst for Water Decomposition. *J. Phys. Chem.* **1988,** *92* (8), 2311-2315.

22. Aruchamy; A, *Photoelectrochemistry and Photovoltaics of Layered Semiconductors*. Kluwer Academic Publishers: Dordrecht, The Netherlands, 1992; Vol. 14.

23. McKone, J. R.; Pieterick, A. P.; Gray, H. B.; Lewis, N. S., Hydrogen Evolution from Pt/Ru-Coated p-Type WSe_2 Photocathodes. *J. Am. Chem. Soc.* **2013,** *135* (1), 223-231.

24. Kline, G.; Kam, K.; Canfield, D.; Parkinson, B. A., Efficient and Stable Photoelectrochemical Cells Constructed with WSe_2 And $MoSe_2$ Photoanodes. *Sol. Energy Mater.* **1981,** *4* (3), 301-308.

25. Wadia, C.; Alivisatos, A. P.; Kammen, D. M., Materials Availability Expands the Opportunity for Large-Scale Photovoltaics Deployment. *Environ. Sci. Technol.* **2009,** *43* (6), 2072-2077.

26. Yu, X. Y.; Sivula, K., Toward Large-Area Solar Energy Conversion with Semiconducting 2D Transition Metal Dichalcogenides. *ACS Energy Lett.* **2016,** *1* (1), 315-322.

27. Pesci, F. M.; Sokolikova, M. S.; Grotta, C.; Sherrell, P. C.; Reale, F.; Sharda, K.; Ni, N.; Palczynski, P.; Mattevi, C., MoS_2/WS_2 Heterojunction for Photoelectrochemical Water Oxidation. *ACS Catal.* **2017,** *7* (8), 4990-4998.

28. Yu, X. Y.; Sivula, K., Photogenerated Charge Harvesting and Recombination in Photocathodes of Solvent-Exfoliated WSe_2. *Chem. Mater.* **2017,** *29* (16), 6863-6875.

29. Chaparro, A. M.; Salvador, P.; Peter, L. M., The Role of Surface-Defects in the Photooxidation of Iodide at n-$MoSe_2$ - Evidence for a Local Autocatalytic Effect. *J. Phys. Chem.* **1995,** *99* (17), 6677-6683.

30. Velazquez, J. M.; John, J.; Esposito, D. V.; Pieterick, A.; Pala, R.; Sun, G. F.; Zhou, X. H.; Huang, Z. Q.; Ardo, S.; Soriaga, M. P.; Brunschwig, B. S.; Lewis, N. S., A scanning probe investigation of the role of surface motifs in the behavior of p-WSe_2 photocathodes. *Energy Environ. Sci.* **2016,** *9* (1), 164-175.

31. Ahmed, S. M.; Gerischer, H., Influence of Crystal-Surface Orientation on Redox Reactions at Semiconducting MoS_2. *Electrochim. Acta* **1979,** *24* (6), 705-711.

32. Lewerenz, H. J.; Gerischer, H.; Lubke, M., Photoelectrochemistry of WSe_2 Electrodes - Comparison Of Stepped And Smooth Surfaces. *J. Electrochem. Soc.* **1984,** *131* (1), 100-104.

33. Eisenberg, D., Imaging the Anisotropic Reactivity of a Tungsten Diselenide Photocathode. *ChemElectroChem* **2015,** *2* (9), 1259-1263.

34. Huang, Y.; Sutter, E.; Shi, N. N.; Zheng, J. B.; Yang, T. Z.; Englund, D.; Gao, H. J.; Sutter, P., Reliable Exfoliation of Large-Area High-Quality Flakes of Graphene and Other Two-Dimensional Materials. *ACS Nano* **2015,** *9* (11), 10612-10620.

35. Chaparro, A. M.; Salvador, P.; Mir, A., The scanning microscope for semiconductor characterization: Photocurrent, photovoltage and electrolyte electroreflectance imaging at the n-$MoSe_2$/I^- interface. *J. Electroanal. Chem.* **1997,** *424* (1-2), 153-157.

36. Tributsch, H.; Sakata, T.; Kawai, T., Photoinduced Layer Phenomenon Caused by Iodine Formation in $MoSe_2$ - Electrolyte (Iodide) Junctions. *Electrochim. Acta* **1981,** *26* (1), 21-31.

37. Turner, J. A.; Parkinson, B. A., The Application of Chronocoulometry to the Study of Adsorption at the Semiconductor Electrolyte Interface. *J. Electroanal. Chem.* **1983,** *150* (1-2), 611-617.

38. Etman, M.; Neumannspallart, M., Critical Analysis of Electrical Contacts to Layered Semiconductors for Use in (Photo)Electrochemical Studies. *J. Electroanal. Chem.* **1989,** *269* (2), 411-422.

39. Gobrecht, J.; Gerischer, H.; Tributsch, H., Electrochemical Solar-Cell Based on the D-Band Semiconductor Tungsten-Diselenide. *Ber. Bunsen-Ges. Phys. Chem. Chemical Physics* **1978,** *82* (12), 1331-1335.

40. Fan, F. R. F.; Bard, A. J., Semiconductor Electrodes .36. Characteristics of n-$MoSe_2$, n-WSe_2 and n-WSe_2 Electrodes in Aqueous-Solution. *J. Electrochem. Soc.* **1981,** *128* (5), 945-952.

41. Salvador, P.; Chaparro, A. M.; Mir, A., Digital imaging of the effect of photoetching on the photoresponse of n-type tungsten diselenide and molybdenum diselenide single crystal electrodes. *J. Phys. Chem.* **1996,** *100* (2), 760-768.

42. Todt, M. A.; Isenberg, A. E.; Nanayakkara, S. U.; Miller, E. M.; Sambur, J. B., Single-Nanoflake Photo-Electrochemistry Reveals Champion and Spectator Flakes in Exfoliated $MoSe_2$ Films. *J. Phys. Chem. C* **2018** *accepted*

43. Tonndorf, P.; Schmidt, R.; Bottger, P.; Zhang, X.; Borner, J.; Liebig, A.; Albrecht, M.; Kloc, C.; Gordan, O.; Zahn, D. R. T.; de Vasconcellos, S. M.; Bratschitsch, R., Photoluminescence emission and Raman response of monolayer MoS_2, $MoSe_2$, and WSe_2. *Opt. Express* **2013,** *21* (4), 4908-4916.

44. Tadayyoni, M. A.; Gao, P.; Weaver, M. J., Application of Surface-Enhanced Raman-Spectroscopy to Mechanistic Electrochemistry - Oxidation Of Iodide At Gold Electrodes. *J. Electroanal. Chem.* **1986,** *198* (1), 125-136.

45. Swietlik, R.; Schweitzer, D.; Keller, H. J., Resonance Raman investigations of the symmetrical stretching mode of I_3^- anions in α and β phases of di-bis(ethylenedithio)tetrathiafulvalene tri-iodide. *Phys. Rev. B* **1987,** *36* (13), 6881-6888.

46. Tributsch, H., Electrochemical Solar-Cells Based on Layer-Type Transition-Metal Compounds - Performance of Electrode Material. *Sol. Energy Mater.* **1979,** *1* (3-4), 257-269.

47. Canfield, D.; Parkinson, B. A., Improvement of Energy-Conversion Efficiency by Specific Chemical Treatments of Normal-$MoSe_2$ and Normal-WSe_2 Photoanodes. *J. Am. Chem. Soc.* **1981,** *103* (5), 1279-1281.

48. White, H. S.; Abruna, H. D.; Bard, A. J., Semiconductor Electrodes .41. Improvement of Performance of n-WSe_2 Electrodes by Electrochemical Polymerization of Ortho-Phenylenediamine at Surface Imperfections. *J. Electrochem. Soc.* **1982,** *129* (2), 265-271.

49. Voiry, D.; Goswami, A.; Kappera, R.; Silva, C.; Kaplan, D.; Fujita, T.; Chen, M. W.; Asefa, T.; Chhowalla, M., Covalent functionalization of monolayered transition metal dichalcogenides by phase engineering. *Nat. Chem.* **2015,** *7* (1), 45-49.

50. Amani, M.; Taheri, P.; Addou, R.; Ahn, G. H.; Kiriya, D.; Lien, D. H.; Ager, J. W.; Wallace, R. M.; Jayey, A., Recombination Kinetics and Effects of Superacid Treatment in Sulfur- and Selenium-Based Transition Metal Dichalcogenides. *Nano Lett.* **2016,** *16* (4), 2786-2791.